Mass sensing by symmetry breaking and localization of motion in an array of electrostatically coupled nonlinear MEMS resonators

Clément C Grenat, Sébastien Baguet, Claude-Henri Lamarque, Régis Dufour

Author manuscript, published in "International Journal of Non-Linear Mechanics", Vol 140, 103903 (2022)
DOI: 10.1016/j.ijnonlinmec.2021.103903
The final publication is available at Elsevier via www.sciencedirect.com

Mass sensing by symmetry breaking and localization of motion in an array of electrostatically coupled nonlinear MEMS resonators

C. Grenat[a], S. Baguet[a,*], C-H. Lamarque[b], R. Dufour[a]

[a] *Univ Lyon, INSA Lyon, CNRS, LaMCoS, UMR5259, 69621 Villeurbanne, France*
[b] *Univ Lyon, ENTPE, CNRS, LTDS, UMR5513, 69518 Vaulx-en-Velin, France*

Abstract

This paper investigates the global dynamics of an array of electrostatically coupled nonlinear MEMS resonators before and after a symmetry breaking event by means of nonlinear normal modes, nonlinear forced responses curves and bifurcation analysis. The possible coexistence of isolated solutions is explained by means of energy balance and limit point tracking. The results show that the energy balance method and limit point tracking can be used equivalently to detect the birth of isolated solutions, but only the limit point tracking can predict accurately their merging. Moreover, the localization of motion and the merging of isolated solutions resulting from a symmetry breaking of the underlying nonlinear normal mode can be exploited to provide alternative mass detection methods. The amount of mass that can be detected by this method is directly related to the initial level of asymmetry.

Keywords: MEMS resonant sensors, Electrostatic coupling, Mass sensing, Nonlinear normal modes, Energy balance, Symmetry breaking, Isolated solution, Bifurcation tracking, Localization of motion

Abbreviation list

BP	Branch point	LP	Limit point
HBM	Harmonic balance method	MEMS	Micro electro-mechanical system
INNM	Isolated nonlinear normal mode	NFRC	Nonlinear forced response curve
IS	Isolated solution	NNM	Nonlinear normal mode

1. Introduction

As presented by Calleja *et al.* [1], nanomechanical sensing is still a scientific challenge. Current research on mass sensing focuses essentially on improving a single resonator. In the last decade, the dimensions of MEMS have been scaled down to sub-micro-metric sizes, thus improving the detection sensitivity up to the zeptogram (10^{-24}kg) [2]. The drawback is the appearance of nonlinear behaviors that can generate adverse dynamical phenomena. However, recent studies tend to take advantage of these nonlinear effects [3–8]. For example, Nguyen *et al.* investigated alternative mass-sensing techniques exploiting nonlinearities [9]. They showed that continuous frequency sweeps performed over a frequency range with multistable solutions lead to hysteresis cycles that can be used to provide a new mass sensing technique with an automatic re-initialization, thus paving the way for real-time detection.

Current technology permits fabricating large arrays composed of a few as well as of thousands of MEMS or NEMS, the dynamics of which results from electrical, magnetic and mechanical couplings. The dynamic behavior of such arrays was studied experimentally or theoretically in [10–12]. For the reader unfamiliar with MEMS arrays, we recommend starting with [13–17]. Arrays of resonant MEMS present a complex dynamic behavior due to the

*Corresponding author. Tel.: +33 4 72 43 81 93; fax: +33 4 78 89 09 80.
Email address: sebastien.baguet@insa-lyon.fr (S. Baguet)

nonlinear couplings induced by electrostatic forces and are still not fully understood. Lifshitz *et al.* [11] used perturbation methods to study the response of a MEMS array under parametric excitation in the weak nonlinear regime. Their results showed that the number of branches of solutions increases significantly with the number of oscillators. Multistability and bifurcations of parametric resonances were also studied by Bitar *et al.* [18, 19]. Modal couplings are another important feature of the dynamics of a beam array. Gutschmidt and Gottlieb [17] analyzed an array with electrical coupling. They focused on the n-beam dynamic behavior in the region of internal one-to-one, parametric and internal three-to-one resonances corresponding to low, medium and large DC voltages. In [20], Kambali *et al.* investigated the extremely complicated nonlinear dynamic regimes and bifurcations of arrays of 5 to 25 elastically coupled hybrid micro cantilever beams subjected to electrodynamic excitation. These nonlinear behaviors are complex to analyze and current work focuses on methods that simplify the understanding of such phenomena. Among these, Hill *et al.* [21] analyzed analytically the appearance of isolated solutions (ISs) supported by nonlinear normal modes (NNMs) and showed that symmetry breaking can generate ISs supported by an isolated NNM (INNM). Kuether *et al.* [22] worked on the energy balance method that provides the amplitude of forcing required to pass by a specific point of a NNM.

Even though current technology permits large arrays of MEMS to be fabricated, such arrays inevitably contain manufacturing defects. To tackle this problem and give MEMS sensors more flexibility in their use, efforts first focused on single tunable MEMS. The recent work by Li *et al.* [23] showed that the nonlinear behavior of MEMS can be tailored to a specific dynamics by means of structural optimization. Two examples of beams were presented. The first one was designed to minimize the cubic nonlinearity while the second one was designed to maximize it. Hajhashemi *et al.* [24] proposed a method to adjust the bandwidth and the resonance frequency of two micro-resonators electrostatically coupled by a middle electrode. Walter *et al.* [25] used a method based on tunable electrostatic actuation and mode localization to compensate manufacturing defects in a single MEMS. Then, several works addressed MEMS arrays. Porfiri [15] showed that the vibrational properties of an array of identical microplates can be tuned by properly adjusting the bias voltage V_{dc} applied across adjacent microplates. Kambali *et al.* [26] focused on understanding the coupling of different modal frequencies and their tuning mechanisms. In the study, modal frequencies were tuned by adjusting V_{dc} in order to obtain specific couplings. Such studies on modal couplings and internal resonances not only permit a better understanding of the dynamics of beam arrays, but also give some insights on specific configurations such as the symmetric one. In the same way, Akgul *et al.* [27] proposed to tune voltages in order to correct the phase and frequency mismatches of a MEMS array. These works offer several possibilities to compensate defects and bring the sensor back into the desired configuration.

With the need for parallel mass sensing and alternative methods for mass detection, the use of MEMS arrays for mass detection received an increased attention. Spletzer *et al.* [28] compared mass sensing methods based on eigenmode changes in a MEMS array with the frequency shift method using a single resonant MEMS sensor. They showed that an added mass on one of the beams of the array affects the shape of the modes. The change was found to be two or three orders of magnitude greater and improved the sensitivity of mass sensing. A mode localization also occurred where the mass was added. Since then, many references proposed to use the mode localization effect as the basis of mass sensing: with linear modes [29–32] or with linear and nonlinear ones [33, 34]. Wang *et al.* [35] used five mechanically coupled beams to perform a mode localization analysis. For a symmetric configuration, the added mass generated a higher amplitude of oscillation on the beams at both ends of the array. In [36], the influence of asymmetry in a MEMS array on mode localization was performed. In [37], Ouakad *et al.* showed that very weak coupling is required to activate mode localization. A review of applications utilizing mode localization is provided by Zhao *et al.* [38]. In a few references, nonlinearities are used to enhance the mode localization effect. In [39], two electrostatically coupled clamped-clamped microbeams of different lengths showed an improved sensitivity when operating in the nonlinear regime. In [40], an array of nonlinear weakly mechanically coupled resonators was considered and an abrupt change in the dynamic behavior due to the mode localization effect was exploited for mass sensing.

In this paper, a symmetric two-beam system is used for mass detection. When an added mass is dropped onto one of the moving beams of the MEMS array, the symmetry of the system is broken. A symmetry breaking event was already used in [41] for mass detection. The present work is based on a different exploitation of symmetry breaking. We first analyze the change in the nonlinear dynamic behavior of the MEMS array before and after symmetry breaking event by means of NNM calculation, bifurcation analysis, limit point (LP) tracking and nonlinear forced response curves (NFRCs). For some configurations of the system, ISs, isolated and mixed NNMs appear. LP tracking is used to catch the various ISs and isolated NNMs. Moreover, the results show that the merging behavior of the ISs with

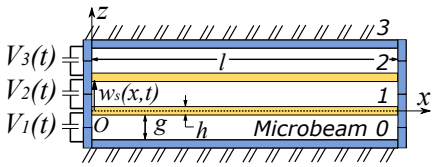

Figure 1: Array of two electrostatically coupled clamped-clamped MEMS beams.

the main response curve depends strongly on the type of NNM that support the ISs. Then, the paper shows how inversion of localization of motion can be used for mass sensing in a two-beam array. The paper is organized as follows. In the first section, the model of the two-beam array is presented. In the second section, the dynamics of the symmetric two-beam array is analyzed via NNMs, energy balance method, frequency response curves and LP tracking. In the third section, a symmetry breaking event is induced by adding a small mass onto the first beam of the array. Then, the dynamics of the two-beam array is analyzed with respect to the asymmetric configuration obtained after the symmetry breaking event. For both symmetric and asymmetric configurations, several phenomena such as localization of motion, merging and birth of ISs are detected and analyzed with respect to in-phase and out-of-phase forcings. Finally, a mass sensing technique based on inversion of localization and in-phase forcing is presented.

2. Array of two micromechanical resonators

Model. A two-moving-beam array is considered, as represented in Fig. 1. The two beams #0 and #3 located at the ends of the array are fixed, i.e., have no lateral motion and serve only for electrostatic actuation. The two middle beams #1 and #2 are clamped at both ends. All beams have identical properties with l, b, h, I, g, E, ρ, Q being respectively the length, width, height, moment of inertia of the beams, gap between two adjacent beams, the Young's modulus, mass density ans quality factor, such as $l = 10\mu m$, $b = 160nm$, $h = 300nm$, $I = bh^3/12$, $g = 200nm$, $E = 1.69 \times 10^{11} N/m^2$, $\rho = 2330 kg/m^3$, $Q = 5000$.
Each beam is an electrostatic actuator for its adjacent beams and the parallel plate approximation [42] is used for the electrostatic force. $V_s = V_{dc}^s + V_{ac}^s \cos(\tilde{\Omega}\tilde{t})$ is the voltage applied between two successive beams $s-1$ and s with V_{dc}, V_{ac} the continuous bias and alternative voltages. The voltages defined in Table 1 will be used in the following to target either the out-of-phase or the in-phase mode.

The bending motion of the beam s in the plane $x-z$ is governed by:

$$EI\frac{\partial^4 \tilde{w}_s(\tilde{x},\tilde{t})}{\partial \tilde{x}^4} + \rho bh\frac{\partial^2 \tilde{w}_s(\tilde{x},\tilde{t})}{\partial \tilde{t}^2} + \delta_i(s)\,\delta_{x_0}(x)\,m\frac{\partial^2 \tilde{w}_s(\tilde{x},\tilde{t})}{\partial \tilde{t}^2} + c\frac{\partial \tilde{w}_s(\tilde{x},\tilde{t})}{\partial \tilde{t}} - \left[\tilde{N}_s + \frac{Ebh}{2l}\int_0^l \left(\frac{\partial \tilde{w}_s(\tilde{x},\tilde{t})}{\partial \tilde{x}}\right)^2 \mathrm{d}\tilde{x}\right]\frac{\partial^2 \tilde{w}_s(\tilde{x},\tilde{t})}{\partial \tilde{x}^2} = \frac{\epsilon_0 b C_n}{2}\left[\frac{V_{s+1}^2}{(g+\tilde{w}_{s+1}-\tilde{w}_s)^2} - \frac{V_s^2}{(g+\tilde{w}_s-\tilde{w}_{s-1})^2}\right] \quad (1)$$

with $s = 1, 2$ and where $\tilde{w}_s$ is the lateral displacement of the s-th beam in the z-direction. The inertial term with the Dirac function represents a small added mass m dropped on beam i at the location x_0. ϵ_0, C_n are the dielectric constant and fringing field coefficient, respectively. $\tilde{N}_s$ is a lineic load along the x-axis resulting from, e.g., manufacturing stresses. Introducing the following non-dimensional parameters:

$$w_s = \frac{\tilde{w}_s}{g}; \quad x = \frac{\tilde{x}}{l}; \quad t = \frac{\tilde{t}}{\tau}; \quad c = \frac{\tilde{c}l^4}{EI\tau}; \quad N_s = \frac{\tilde{N}_s l^2}{EI}; \quad \alpha_1 = 6(\frac{g}{h})^2; \quad \alpha_2 = 6C_n\frac{\epsilon_0 l^4}{Eh^3 g^3}; \quad \Omega = \tilde{\Omega}\tau; \quad \delta_m = \frac{m}{\rho bhl} \quad (2)$$

in Eq. (1), yields:

$$\frac{\partial^4 w_s}{\partial x^4} + (1+\delta_i(s)\,\delta_{x_0}(x)\,\delta_m)\frac{\partial^2 w_s}{\partial t^2} + c\frac{\partial w_s}{\partial t} - \left[N_s + \alpha_1\int_0^1 (\frac{\partial w}{\partial x})^2 \mathrm{d}x\right]\frac{\partial^2 w_s}{\partial x^2} = \alpha_2\frac{V_{s+1}^2}{(1+w_{s+1}-w_s)^2} - \alpha_2\frac{V_s^2}{(1+w_s-w_{s-1})^2}. \quad (3)$$

with $s = 1, 2$.

Type of forcing	V_{dc}^1	V_{ac}^1	V_{dc}^2	V_{ac}^2	V_{dc}^3	V_{ac}^3	Targeted mode in Fig.2a
Out-of-phase forcing	3	0.1	3	0	3	0.1	Out-of-phase mode ①
In-phase forcing	3	0.1	3	0	3	-0.1	In-phase mode ②

Table 1: Applied voltages.

Static equilibrium and pull-in voltages. The static equilibrium of the system is studied by setting all time dependent terms in (3) to zero. Two pull-in instabilities are found for $V_{dc}^{crit} = 41.1$V and $V_{dc}^{crit} = 71.3$V. The V_{ac} voltage also contributes to the static equilibrium via the constant term of the squared cosine of the electrostatic force. Nevertheless, it is found that its contribution to the pull-in is negligible. Therefore, it can be concluded that the voltages defined in Table 1 are well below the critical pull-in voltage V_{dc}^{crit}.

General methodology for the dynamic analysis. Since the resonators #1 and #2 of the two-beam arrays are identical, their linear undamped eigenmodes are the same. One linear mode is used in the Galerkin method to remove the spatial dependence from Eq. (3). The periodic solutions of the resulting set of nonlinear differential equations are computed numerically with the Harmonic Balance Method (HBM) [43]. The NNMs are computed as solutions of the phase resonance equation defined in [44]. This equation being autonomous, a phase condition is added and the equation of motion are regularized to ensure the computation of a unique solution. Then the stability and bifurcation points of the NNM are calculated using a regularized quadratic eigenvalue problem and an augmented system. An energy balance is performed to calculate the corresponding amplitude of the force necessary to pass by a given point of the NNM [22]. Since some of these procedures are used extensively in the present paper but are not found in the available numerical continuation packages, a homemade Matlab software was developed. It permits classical continuation, stability analysis, detection and tracking of bifurcations and energy balance. A convergence study has shown that using $H = 5$ harmonics for the HBM, Taylor series at order 7 for approximating the electrostatic forcing and $N_m = 1$ mode for the Galerkin method is a good compromise between accuracy of the results and reasonable computational time.
Finally, it should be noted that $\rho bhl = 1.1184 \times 10^{-15} kg$. Therefore, the non-dimensional additional mass $\delta_m = 10^{-4}$ used in this paper corresponds to a physical mass $m = 1.1184 \times 10^{-19} kg$.

3. Dynamics of the perfectly symmetric system

In this section, the dynamics of the symmetric two-beam MEMS system is analyzed by means of NNM, energy balance, nonlinear forced response curves (NFRCs) and LP tracking. Several phenomena such as bifurcating NNM, localization of motion, merging and birth of ISs are detected and explained. In section 3.1, the NNMs of the system are computed. The energy balance method is explained and applied to the electrostatically actuated two-beam array. In Section 3.2, the dynamics of the system is analyzed with respect to an electrostatic forcing targeting the out-of-phase NNM. Finally in Section 3.3, the dynamics of the system is analyzed with respect to an electrostatic forcing targeting the in-phase NNM.

3.1. NNM computation and link with periodic forced responses

In this subsection, the NNMs of the two-beam system in symmetric configuration are computed. Then, the energy balance method is explained and applied to the two-beam system. In the following, all computations are carried out with electrostatic forces using the voltages listed in Table 1. For these levels of electrostatic forcing, no softening behavior is present in the frequency response curves. For higher values of V_{ac}, a transition from hardening to softening behavior may be observed at large amplitudes, leading to dynamic pull-in instability, but this case is beyond the scope of this paper. The system exhibits two main NNM branches, also called pure NNMs, which are initialized at null amplitude using the linear eigenfrequencies and modal shapes, as shown in Fig 2a. The first and second pure NNMs correspond to the out-of-phase and in-phase NNMs respectively. The modal displacement of these NNMs are represented in Fig. 2b for explanatory purposes. One can see that a branch point (BP) is present on the pure in-phase NNM initialized at the non-dimensional frequency $\Omega = 22.35$, see Fig. 2a. Beyond this BP, the pure NNM becomes unstable and a stable mixed NNM appears. The terminology *pure* and *mixed* NNM is taken from [45]. A

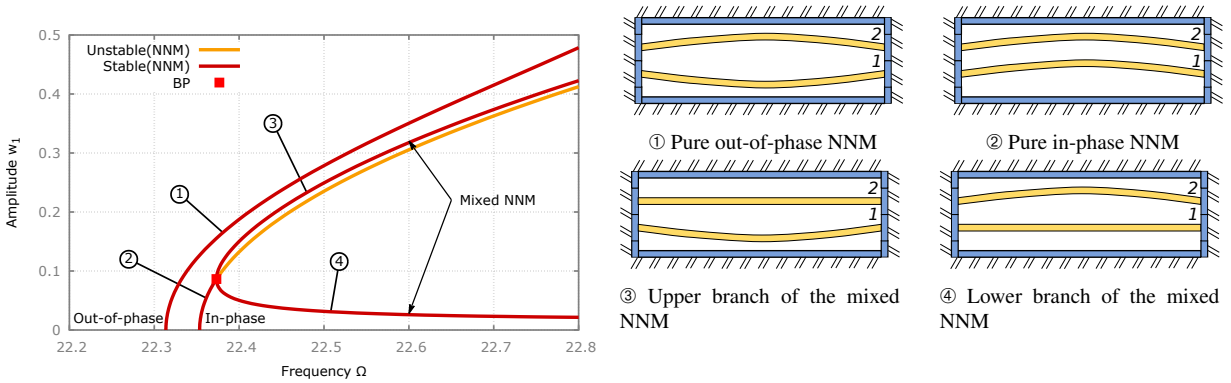

(a) Amplitude w_1 at mid-point of beam #1

(b) Schematic representation of the modal displacements

Figure 2: NNMs of the MEMS array in the perfectly symmetric case ($\delta_m = 0$). ①: out-of-phase NNM, ②: in-phase NNM, ③ and ④: mixed NNM.

mixed NNM has an asymmetric modal shape made of a mix of pure NNM modal shapes. This can be seen on their respective modal displacements in Fig. 2b. The modal displacement of the upper and lower parts of the mixed NNM present respectively high and low amplitude of displacement of beam #1 as seen in Fig. 2a. Since the beam array is symmetric, the upper and lower part of the mixed NNM would respectively become the lower and the upper part on a figure displaying the amplitude of beam #2. Indeed, one can see in Fig. 2b that the amplitudes of beam #2 are low for the upper part of the mixed NNM and high for its lower part . Consequently, the NNM analysis is relevant for the nonlinear analysis of a symmetric system because it can reveal the presence of asymmetric responses.

The NNM branches serve as so-called backbone curves for the NFRCs, i.e., they support the NFRCs, and their intersection with the NFRCs corresponds to the phase resonance of the NFRCs. The NFRC intersecting a specific point of a NNM branch can be identified by applying the energy balance method. This method consists in finding which electrostatic forcing has to be applied to the system so that the energy injected in the system balances the dissipated energy. The dissipating forces are given by:

$$\boldsymbol{F}_{dis} = (\nabla \otimes \boldsymbol{C})\,\boldsymbol{X} \tag{4}$$

with ∇ the frequency-domain differential operator, $\otimes$ the Kronecker tensor product, $\boldsymbol{C}$ the damping matrix of the underlying linear system and $\boldsymbol{X}$ the vector of Fourier coefficients of the displacement w [43]. The only forces that inject energy into the system are the electrostatic forces in the r.h.s. of (3). The voltages indicated in Table 1 are taken as reference and a coefficient d is used to scale the V_{ac} voltage:

$$V = V_{dc} + d\,V_{ac}\cos(\Omega t) \tag{5}$$

The electrostatic forces can then be decomposed in three terms proportional to $1, \cos(\Omega t), \cos(2\Omega t)$ as follows:

$$\begin{aligned} f_e(x,t) = \alpha_2 \left(\frac{V_{dc}^{s+1\,2} + \frac{d^2}{2} V_{ac}^{s+1\,2}}{(1 + w_{s+1} - w_s)^2} - \frac{V_{dc}^{s\ 2} + \frac{d^2}{2} V_{ac}^{s\ 2}}{(1 + w_s - w_{s-1})^2} \right) + 2\alpha_2 d \left(\frac{V_{dc}^{s+1} V_{ac}^{s+1}}{(1 + w_{s+1} - w_s)^2} - \frac{V_{dc}^{s} V_{ac}^{s}}{(1 + w_s - w_{s-1})^2} \right) \cos(\Omega t) \\ + \alpha_2 d^2 \left(\frac{1}{2} \frac{V_{ac}^{s+1\,2}}{(1 + w_{s+1} - w_s)^2} - \frac{1}{2} \frac{V_{ac}^{s\ 2}}{(1 + w_s - w_{s-1})^2} \right) \cos(2\Omega t) \end{aligned} \tag{6}$$

Within the HBM framework, these terms generate three vectors $\boldsymbol{F}_0, \boldsymbol{F}_1, \boldsymbol{F}_2$ which are the contributions to the constant term, the first harmonics Ω and the second harmonics 2Ω of the Fourier series. $\boldsymbol{F}_0$ being a conservative force, it is discarded from the energy balance equation. Finally, the energy balance can be expressed as:

$$\boldsymbol{X}^T \left(\nabla^2 \otimes \boldsymbol{C} \right) \boldsymbol{X} = d\boldsymbol{X}^T (\nabla \otimes \boldsymbol{I})\,\boldsymbol{F}_1 + d^2 \boldsymbol{X}^T (\nabla \otimes \boldsymbol{I})\,\boldsymbol{F}_2 \tag{7}$$

where the l.h.s. corresponds to the dissipated energy and the r.h.s. to the injected energy. At each point of a NNM branch, the $\boldsymbol{X}$ vector is known and the multiplier coefficient d can be computed from (7). The NFRC corresponding

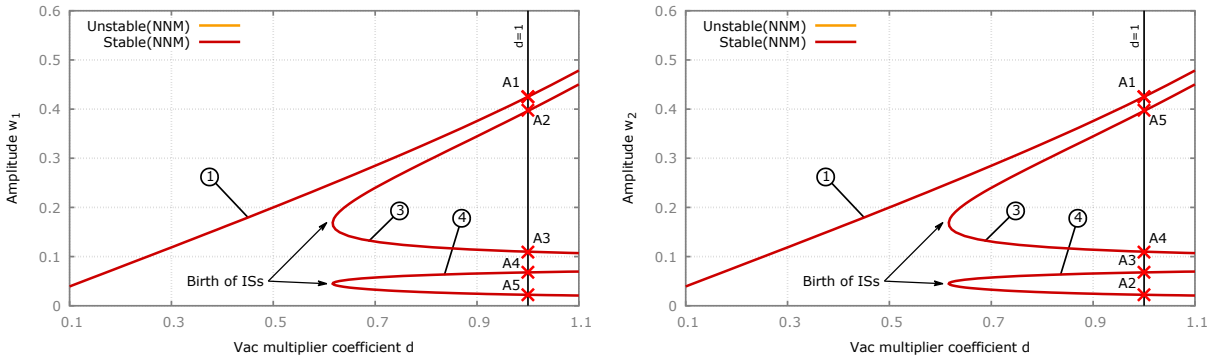

(a) Beam #1

(b) Beam #2

Figure 3: Out-of-phase forcing - Energy balance in symmetric case ($\delta_m = 0$ on beam #1). ①: out-of-phase NNM, ③ and ④: mixed NNM.

to this level of electrostatic forcing can then be computed. It will be shown in the next sections that, when the NFRC is supported by a unique NNM, it will have its phase resonance exactly at the NNM point, i.e., it will intersect the NNM exactly at this point. When the NFRC is supported by several NNMs, it will not intersect the NNM exactly at this point. In this case, the NNM point represents the modal contribution of the considered NNM.

The out-of-phase NNM is targeted with a forcing vector respecting the symmetry of the mode, as defined in Table 1. The energy balance method and NFRCs are used to analyze the dynamics of the two-beam array which exhibits phenomena such as localization of motion, merging and birth of ISs.

3.2. Isolated solutions in the case of out-of-phase forcing

The value of the multiplier coefficient d corresponding to a given NNM amplitude and resulting from the energy balance of Eq. (7) in the case of the "out-of-phase" voltages of Table 1 is plotted in Fig. 3. This plot can be read in two ways. For a given amplitude w, it provides the forcing level d to be used for the NFRC to cross the NNM at this amplitude w. Alternatively, for a given value of the forcing parameter d, it provides the amplitudes w at which the NFRC computed for this forcing level d crosses the NNMs. The pure out-of-phase NNM presents a standard behavior. Its amplitude increases multiplier coefficient d increasing. The mixed NNM presents an asymptotic behavior when it approaches the BP, i.e., an infinite multiplier coefficient d is needed to reach the BP. This behavior is the direct consequence of the two pure NNMs being orthogonal to each other in symmetric configuration. For $d = 1$, the mixed NNM is crossed at four points $(A2, A3, A4, A5)$. Therefore, IS branches are found on each branch of the mixed NNM. Even though the two-beam array is symmetric, the points $(A2, A3, A4, A5)$ are not found at the same location on the NNMs for each beam due to asymmetric modal shape of the mixed NNM. This behavior is also known as localization of motion.

The NRFCs of Fig. 4 are computed subject to the out-of-phase forcing as defined in Table 1. The out-of-phase NNM and the mixed NNM are strongly excited with the out-of-phase forcing while the in-phase NNM does not respond due to the orthogonality of the two modes. As a consequence, the main NFRC is supported by the out-of-phase NNM and two ISs are supported by the two branches of the mixed NNM. The points $(A1, A2, A5)$ are superimposed with LPs contrarily to the two points $(A3, A4)$ closer to the in-phase NNM. The transitions between stable and unstable branches other than LP correspond to Neimark-Sacker bifurcations. They are not plotted for the sake of readability of the figure and because they do not serve the purpose of this paper. The frequency and Fourier coefficients of the displacement vectors of the NNMs at points $(A2, A5)$ are used to initialize the computation of the ISs. The IS initialized with point $A2$ has a high amplitude for beam #1 and a low amplitude for beam #2. The IS initialized with point $A5$ shows a complementary localization of motion with low amplitudes for beam #1 and high amplitude for beam #2. The phenomenon of localization of motion is well visualized with the energy balance method.

In next section, the in-phase NNM is targeted with the in-phase forcing of Table 1. Energy balance method and NFRCs are used to analyze the dynamic of the two-beam array with in-phase forcing. Localization of motion, merging and birth of ISs are explained with respect to the symmetric configuration and the in-phase forcing.

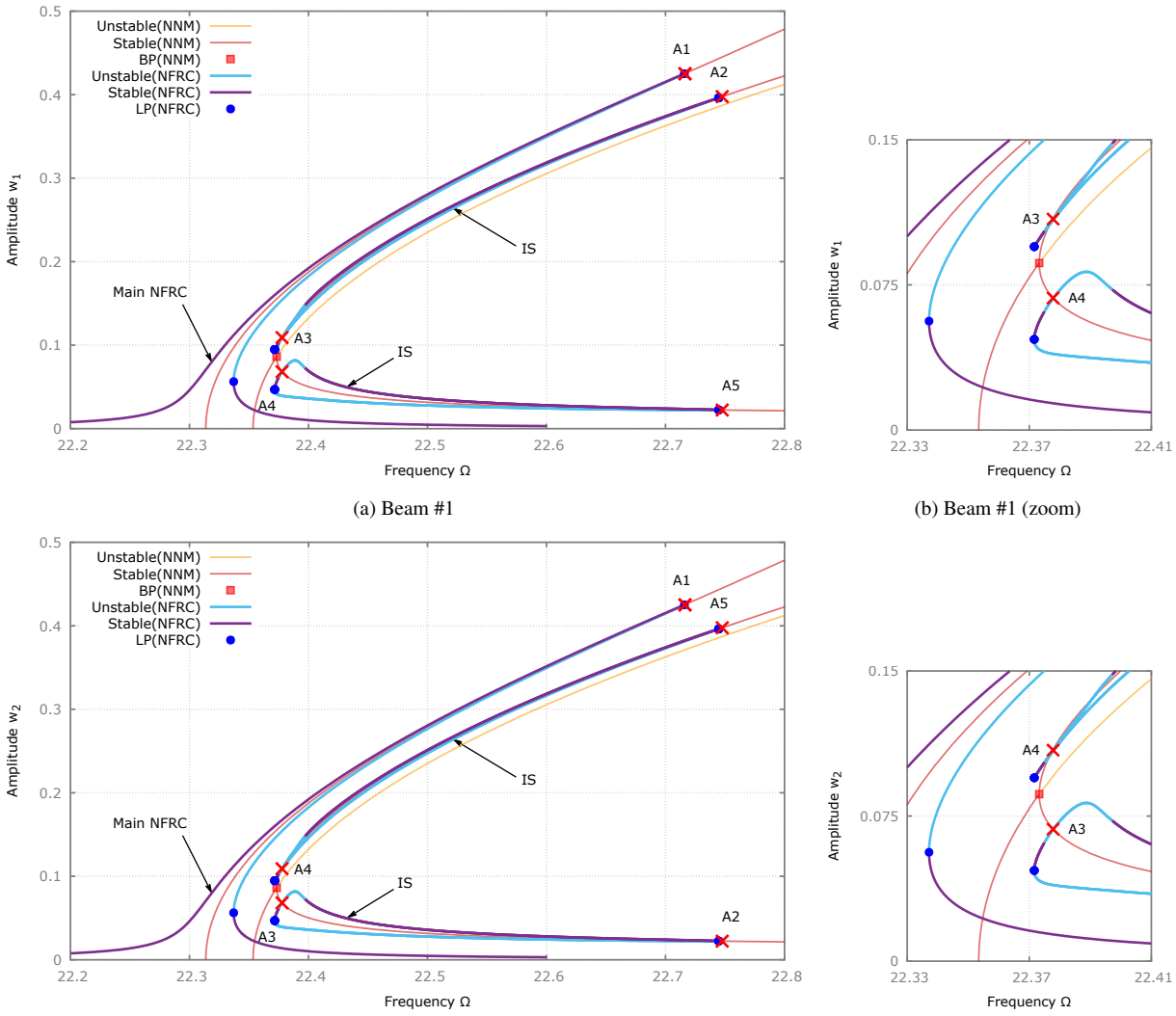

(a) Beam #1

(b) Beam #1 (zoom)

(c) Beam #2

(d) Beam #2 (zoom)

Figure 4: Out-of-phase forcing ($d = 1$) - NFRCs and ISs in symmetric case ($\delta_m = 0$ on beam #1)

3.3. Bifurcated solutions in the case of in-phase forcing

The value of the forcing coefficient d resulting from the energy balance of Eq. (7) in the case of the in-phase forcing of Table 1 is plotted in Fig. 5. The in-phase NNM follows a standard behavior. Its amplitude increases with increased coefficient d. The mixed NNM starts to be excited for $d \simeq 0.22$ and at the same amplitude as the BP of Fig. 2. Thus, the energy level required to excite the BP can be viewed as the threshold above which the mixed NNM is excited. The fact that the BP can be excited also indicates that the solutions existing on both sides of the mixed NNM can merge. For higher values of d, the upper part of the mixed NNM increases with d. The difference in amplitude between the in-phase NNM and the upper part of the mixed NNM tends to a constant value as d increases. The lower part of the mixed NNM decreases as d increases, leading to an increasing difference of amplitude between the lower part of the mixed NNM and the in-phase NNM. For $d = 1$, the mixed NNM is crossed at two points ($B1, B3$). Those points are not found at the same location on both beams. Point $B1$ presents high amplitude on beam #1 and low amplitude on beam #2, whereas point $B3$ shows a complementary behavior with a low amplitude on beam #1 and a high amplitude on beam #2. As with the out-of-phase forcing, the mixed NNM shows localization of motion.

The NFRCs of Fig. 6 are computed subject to the in-phase forcing of Table 1. For the sake of clarity, the main

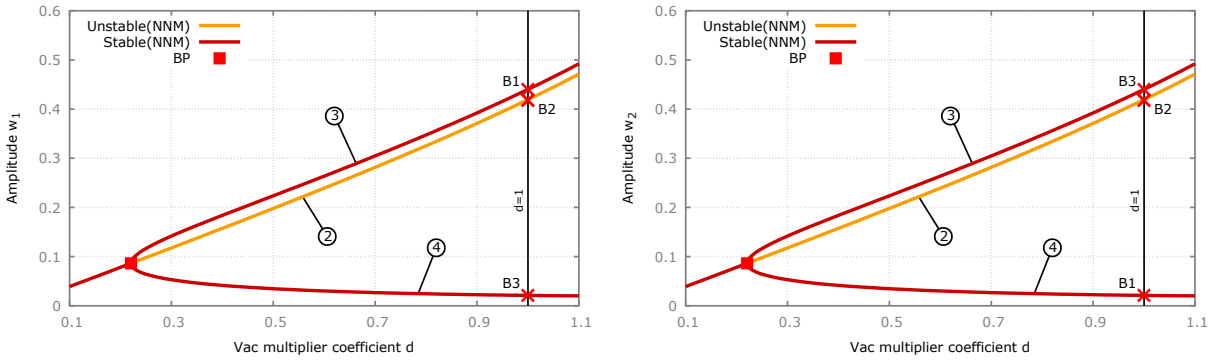

(a) Beam #1 (b) Beam #2

Figure 5: In-phase forcing - Energy balance in symmetric case ($\delta_m = 0$ on beam #1). ②: in-phase NNM, ③ and ④: mixed NNM.

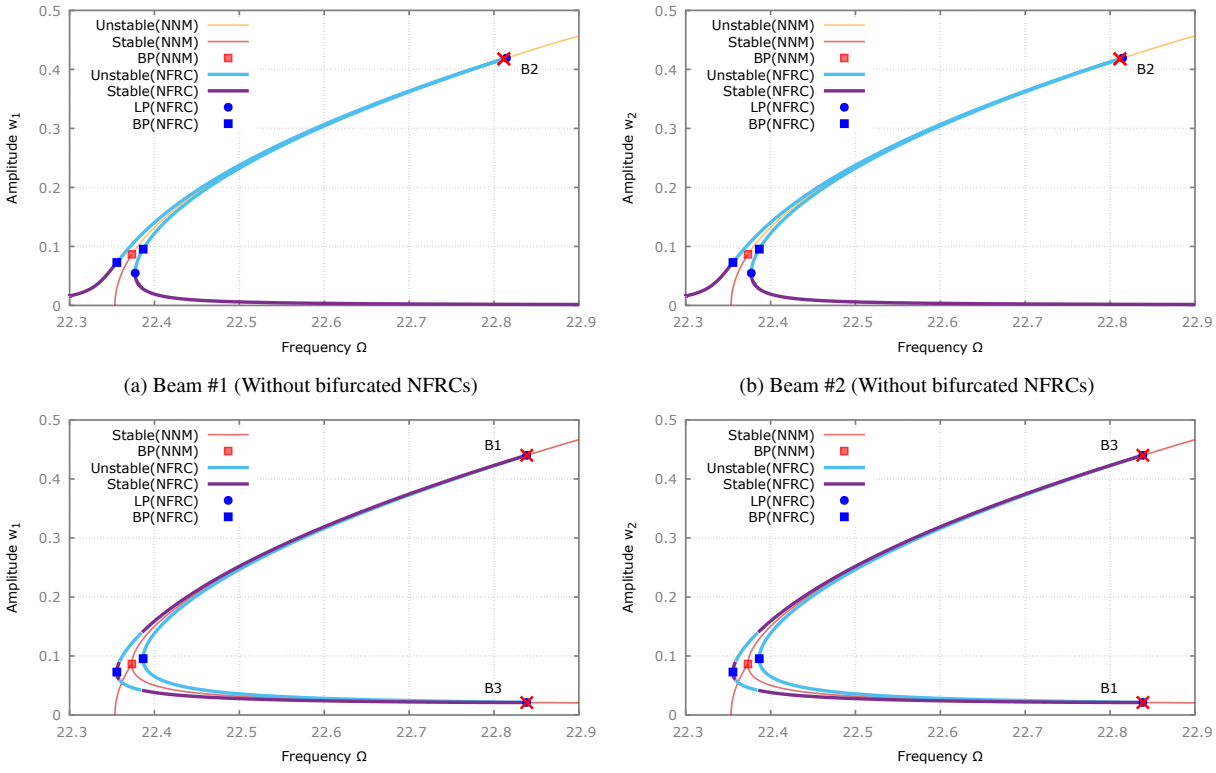

(a) Beam #1 (Without bifurcated NFRCs) (b) Beam #2 (Without bifurcated NFRCs)

(c) Beam #1 (Bifurcated NFRCs only) (d) Beam #2 (Bifurcated NFRCs only)

Figure 6: In-phase forcing ($d = 1$) - NFRCs and ISs in symmetric case ($\delta_m = 0$ on beam #1)

NFRCs supported by the pure NNM and the bifurcated NFRCs by the mixed NNM are plotted separately. The in-phase NNM is well targeted with the in-phase V_{ac} voltages. The out-of-phase NNM does not respond due to the orthogonality of the two modes. On the stable part of the excited pure NNM, the NFRCs are stable until BPs are encountered, see Fig. 6a. Then, the NFRCs become unstable and are supported by the unstable part of the NNM. The BPs encountered onto the NFRCs correspond to symmetry-breaking bifurcations. Additional branches of NFRCs emanate from these BPs, see Fig. 6c. Since they are supported by a mixed NNM, these NFRCs do not correspond to symmetric responses anymore. The ends of those branches coincide with points $B1$ and $B3$. In Fig. 6c, $B1$ is at

high amplitude and $B3$ at low amplitude, whereas $B1$ is at low amplitude and $B3$ at high amplitude in Fig. 6d, which confirms the localization of motion predicted by the energy balance method.

Before switching to the asymmetric case in the next section, observations concerning the perfectly symmetric case are briefly summarized. In symmetric configuration, NNMs of the MEMS array are composed of mixed and pure NNMs. Mixed NNMs are bifurcated branches emerging from the BPs located on pure NNMs. The mixed NNM mode shapes are a mix of pure NNM mode shapes and present localization of motion. When the pure NNM from which the mixed NNM branches emerge is not excited, the ISs cannot merge with the main NFRC for any amplitude of forcing. When the pure NNM from which the mixed NNM branches emerge is excited, the ISs will merge with the main NFRC for a high enough amplitude of forcing, leading to bifurcated NFRCs. If the pure NNM from which the mixed NNM branches emerge the mixed NNM is excited enough compared to the others NNMs composing the mixed NNM, then the NFRCs supported by the mixed NNM appear only as bifurcated solutions and not as ISs.

4. Dynamics with broken symmetry due to an added mass

In this section, symmetry breaking is generated by adding a dimensionless mass ($\delta_m = 10^{-4}$) on beam #1. The dynamics of the resulting asymmetric MEMS array is analyzed by mean of NNM, energy balance, NFRCs and LP tracking. Phenomena such as isolated NNMs (INNMs), localization of motion, birth and merging of ISs are analyzed and compared to results obtained in the previous section for the symmetric case.

4.1. Influence of symmetry breaking on the NNMs

The NNMs of the beam array with the added mass are plotted in Fig. 7. As expected, the symmetry breaking transforms the BP of Fig. 2 into an imperfect bifurcation. As a result, the mixed and symmetric pure NNMs are turned into an INNM and an asymmetric pure NNM and the BP is transformed into an LP as depicted in Fig. 8. To verify the presence of the INNM, an LP-bifurcation tracking with respect to the dimensionless added mass δ_m

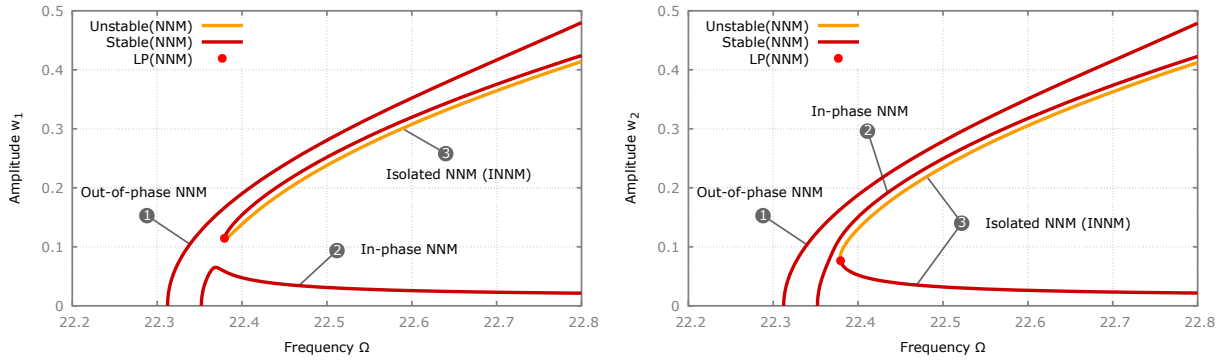

(a) Beam #1 (b) Beam #2

Figure 7: NNMs with their isolated branches (INNMs) after symmetry breaking ($\delta_m = 10^{-4}$ on beam #1). ❶: out-of-phase NNM, ❷: in-phase NNM, ❸: isolated NNM.

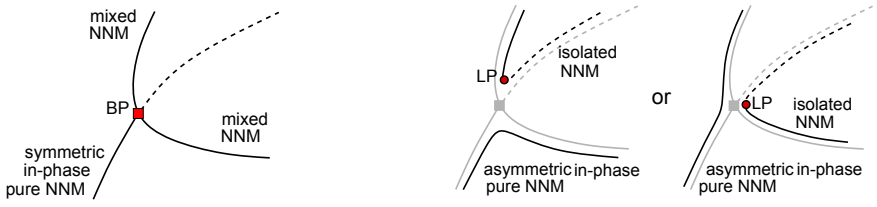

(a) Perfect bifurcation (b) Imperfect bifurcation

Figure 8: Schematic representation of a perfect (a) and imperfect (b) bifurcation. Depending on the sign/direction of the imperfection, the perfect bifurcation is broken into the first or second imperfect case.

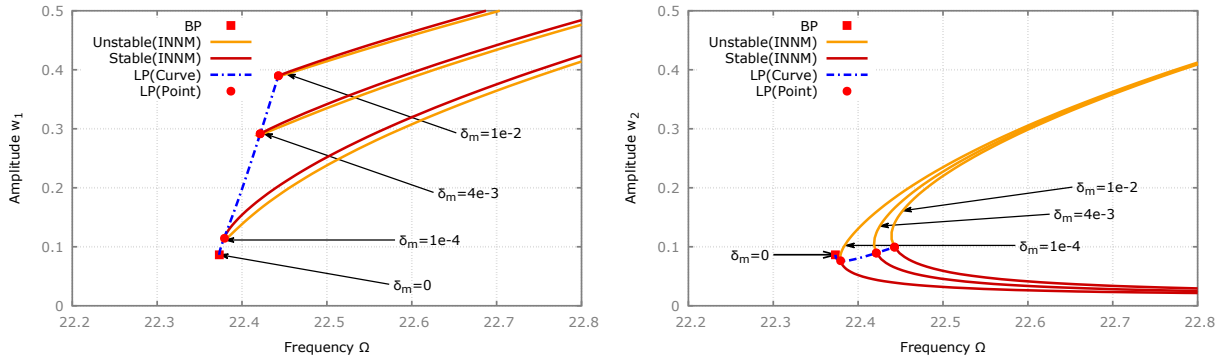

(a) Beam #1 (b) Beam #2

Figure 9: Bifurcation tracking of LPs with respect to δ_m for the characterization of isolated branches of NNMs (INNMs)

is performed, see Fig. 9. This is done by considering δ_m as an unknown and adding to the equation of motion an equation characterizing LP bifurcations [43]. The solutions of such an augmented system are LP bifurcations only and their continuation provides a codim-2 LP branch. The LP tracking is started at $\delta_m = 0$ which corresponds to the BP of the perfectly symmetric case of the previous section. All points of the tracking curve for $\delta_m \neq 0$ are LPs of INNMs. These LPs can be used to initialize the continuation of the INNM of interest. With the added mass on beam #1, the dynamics of the in-phase NNM is completely changed. The BP has disappeared and the in-phase NNM is now different for each beam. Regarding beam #1, the in-phase NNM is composed of the lower part of the in-phase NNM and lower branch of the mixed NNM of Fig. 3. Moreover, since it is now asymmetric, each beam has different modal displacements. Regarding beam #2, the in-phase NNM is composed of the left part of the perfect in-phase and mixed NNMs of Fig. 2. A phenomenon of localization of motion can be observed. The amplitude of motion of the in-phase NNM is lower for beam #1 with added mass than for beam #2. For beam #1, the INNM is composed of the upper part of the in-phase and mixed NNMs from Fig. 3, while for beam #2, the INNM is composed of the right part of the in-phase and mixed NNMs from Fig. 3. In Fig. 9, the LP tracking with respect to the dimensionless added mass δ_m reveals that the INNM moves away from the location of the previous BP as the added mass increases.

4.2. Influence of symmetry breaking on forced responses in the case of out-of-phase forcing

Isolated solutions and localization of motion. In order to target the out-of-phase mode in the asymmetric case, the out-of-phase electrostatic forcing of Table 1 is used. The multiplier coefficient d resulting from the energy balance defined in Section 3.1 is plotted in Fig. 10. The out-of-phase mode follows a standard behavior up to 60% of the initial gap ($w_1 \simeq 0.6$): the response amplitude increases with increased forcing amplitude d. Above 60% of the gap, the high electrostatic forces cause an exponential increase of amplitude. On the other hand, the behavior of the in-phase mode and INNM is more unusual. They both present a limit point where ISs appear (birth of ISs) and are both subject to pull-in at around 80% of the initial gap ($w_1 \simeq 0.8$). Since there is no branch point connecting the NNMs and the INNM in Fig. 10, it can be expected that the ISs supported by the INNM will never merge with the main NFRC for any amplitude of forcing. On the other hand, the in-phase NNM presents another type of merging point that occurs at $d \simeq 2.4$ and will be discussed in the next paragraph. For an arbitrary choice of $d = 1$, four points ($C2, C3, C4, C5$) are found on the mixed NNM and two points ($C1, C6$) on the pure NNMs. The points ($C1, C2$) are located on the out-of-phase and the in-phase NNMs respectively. The presence of point $C6$ shows that the in-phase NNM is also excited by the out-of-phase forcing, but with a very limited contribution. This is due to the slightly asymmetric configuration induced by the symmetry breaking.

The NFRCs corresponding to this forcing amplitude $d = 1$ are plotted in Fig. 11. It can be observed that the localization of motion is still present: the positions of points ($C2, C3$) and ($C4, C5$) are inverted when considering either beam #1 or beam #2. The two points ($C2, C5$) found on the mixed NNM for $d = 1$ are used to initialize the ISs. The IS initialized with $C2$ is supported by the stable part of the INNM only. The IS initialized with $C5$ is supported by the in-phase NNM. It can be observed that points $C2$ and $C5$ coincide perfectly with LPs, whereas points $C3$ and

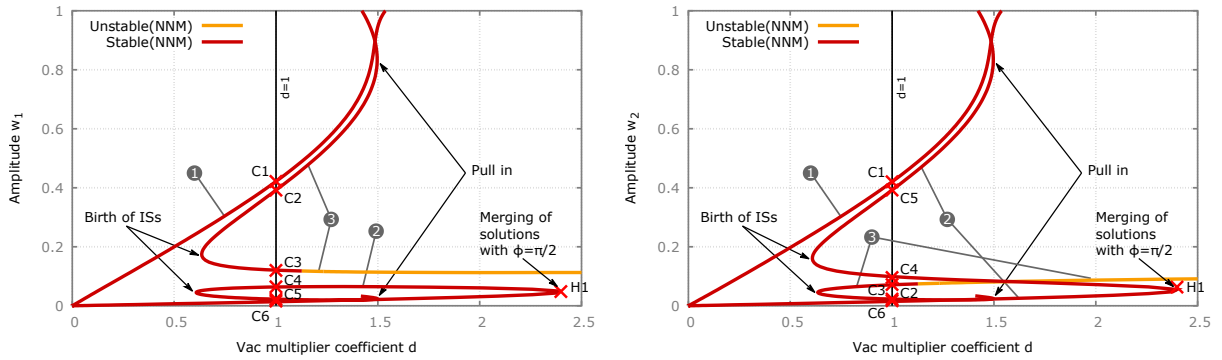

(a) Beam #1 (b) Beam #2

Figure 10: Out-of-phase forcing - Energy balance after symmetry breaking ($\delta_m = 10^{-4}$ on beam #1). ❶: out-of-phase NNM, ❷: in-phase NNM, ❸: isolated NNM.

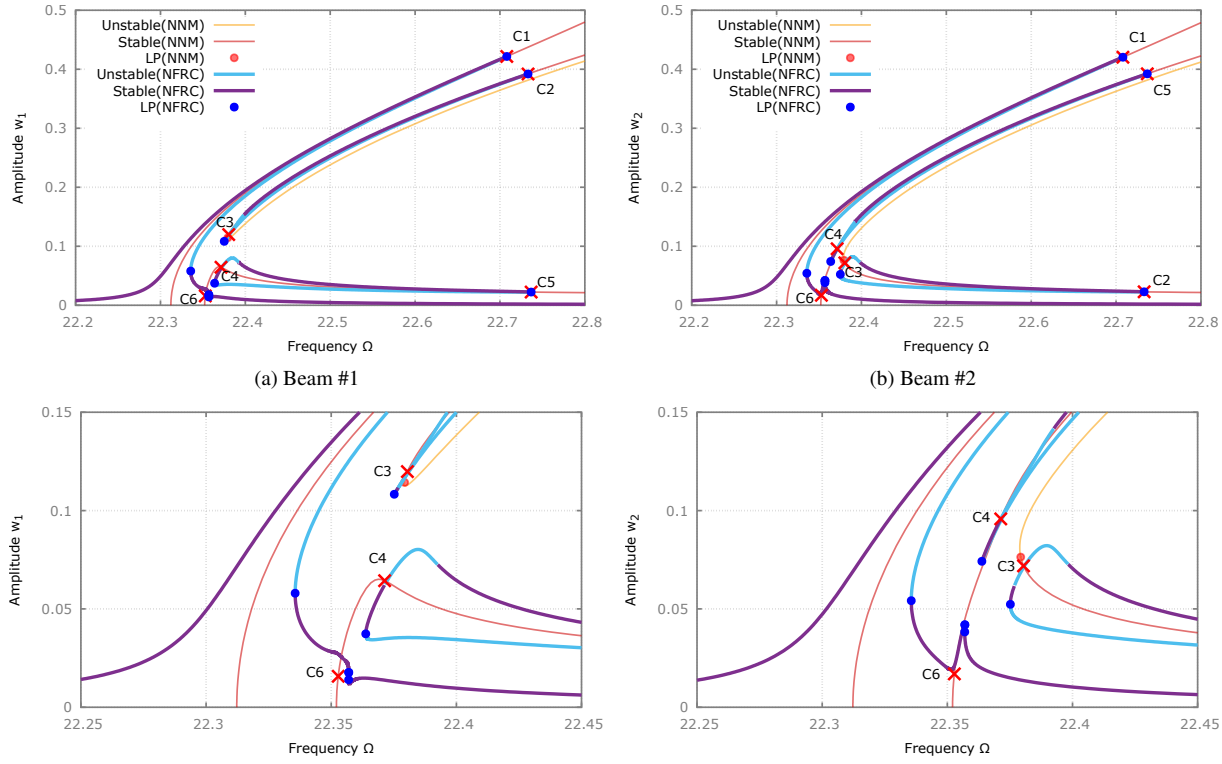

(a) Beam #1 (b) Beam #2

(c) Beam #1 (zoom) (d) Beam #2 (zoom)

Figure 11: Out-of-phase forcing ($d = 1$) - NFRCs and ISs after symmetry breaking ($\delta_m = 10^{-4}$ on beam #1)

$C4$ do not. This indicates that LP tracking and energy balance can be used equivalently to detect the birth of ISs. On the other hand, this also suggests that the two methods will characterize two different types of merging behavior.

Birth and merging of isolated solutions. In order to verify this assumption, the results of the two methods are compared. First, a LP bifurcation tracking is performed with respect to the multiplier coefficient d, starting from point $F1$ on the main NFRC. This is done by considering d as an unknown and performing the continuation of the LP branch characterized by an augmented system [43]. It can be verified in Figs. 12a and 12b that this LP branch passes by the two LPs $F2$ and $F3$ of the bottom IS. In Figs. 12c and 12d, the number of LPs for a given value of d is provided

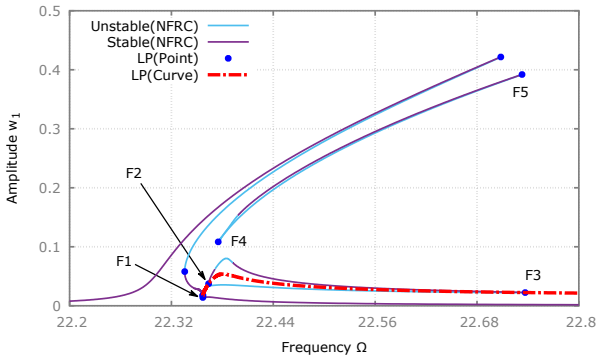

(a) Beam #1

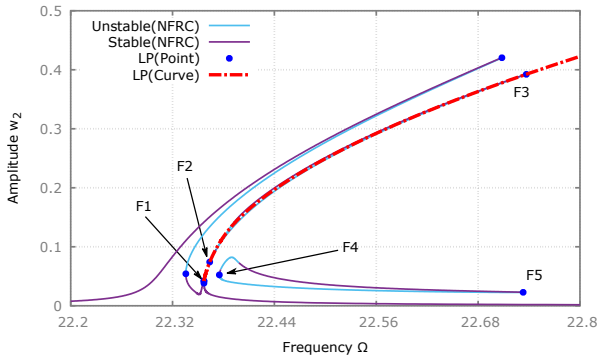

(b) Beam #2

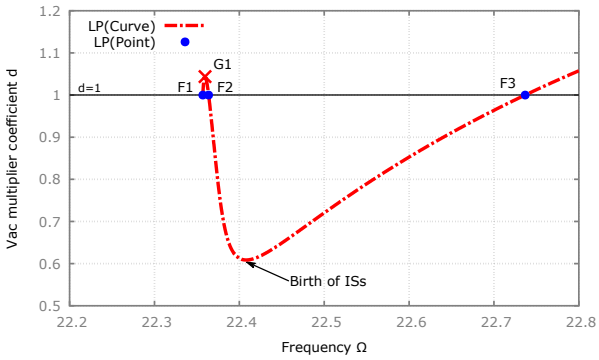

(c) LP tracking in the d-Ω plane

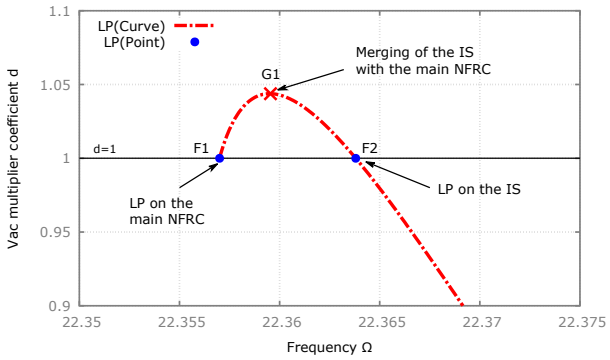

(d) LP tracking in the d-Ω plane (Zoom of Fig. 12c)

Figure 12: Out-of-phase forcing ($d = 1$) - NFRCs after symmetry breaking ($\delta_m = 10^{-4}$ on beam #1) + LP tracking with respect to the forcing coefficient d.

by the intersections with the LP branch. For $d = 1$, in addition to the LP $F1$ which belongs to the main NFRC, two other LPs $F2$ and $F3$ are found. They do not belong to the main NFRC but to the IS, as verified in Figs. 12a and 12b. Therefore, the LP tracking can be used to detect the presence of ISs, and the corresponding IS can be computed by means of a continuation method with a LP as starting point. Moreover, since the LPs of the main NFRC and those of the IS belong to the same LP branch, one can expect to see the main NFRC and the IS merge for some value of d. Conversely, the two LPs $F4$ and $F5$ on the upper IS supported by the INNM were not found during this LP tracking. This indicates that they belong to a different LP branch which is disconnected from the main NFRC. As a consequence, this IS will never merge with the main NFRC for any forcing amplitude d in the case of out-of-phase forcing. The forcing amplitudes corresponding to the birth and merging points of ISs can be deduced from the LP tracking. According to Fig. 12c, the minimum multiplier coefficient necessary for an IS to appear is $d \approx 0.6$. Since this value is the same as with the energy balance method (see Fig. 10), it can be concluded that both the LP tracking and the energy balance method are relevant for assessing the birth of ISs. Concerning the merging behavior, the ISs and the main NFRC merge for $d_{merging} \simeq 1.05$ (point $G1$ on Fig. 12) which is smaller than the merging value $d \simeq 2.45$ found with the energy balance (point $H1$ of Fig. 10). It is worth mentioning that merging of IS can also occur when δ_m is changed, as explained is Section 5 and shown in Figs. 18 and 21.

In order to verify that merging has actually occurred, the NFRC is computed for an out-of-phase forcing amplitude $d = 1.06$ slightly above $d_{merging}$ and plotted in Fig. 13. For the sake of clarity, the ISs supported by the INNM are not plotted as they do not merge with the main NFRC. One can see that the IS and the main NFRC have merged near point $G1$ obtained from LP tracking. This figure is to be compared with Fig. 11a which corresponds to the state before merging and where the IS and the main NFRC are separated by some cut near point $G1$. This validates the fact that LP tracking is able to characterize the merging of ISs with the main NFRC.

Once the ISs have merged with the main NFRC, a phenomenon of localization of motion can be observed for

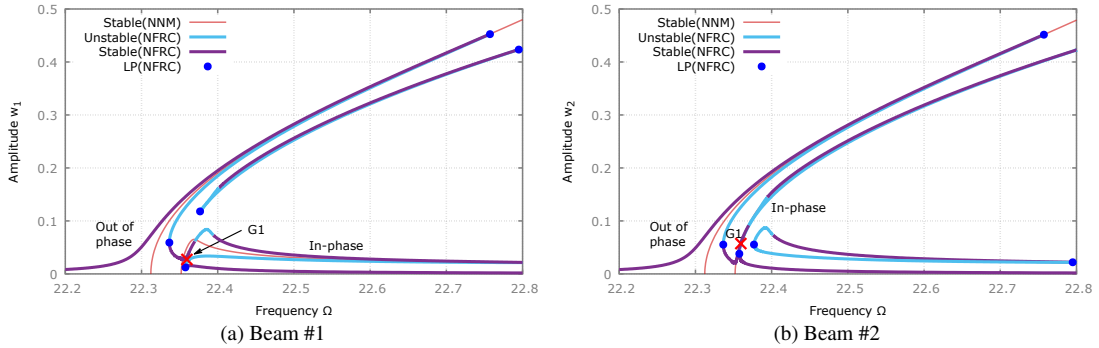

(a) Beam #1 (b) Beam #2

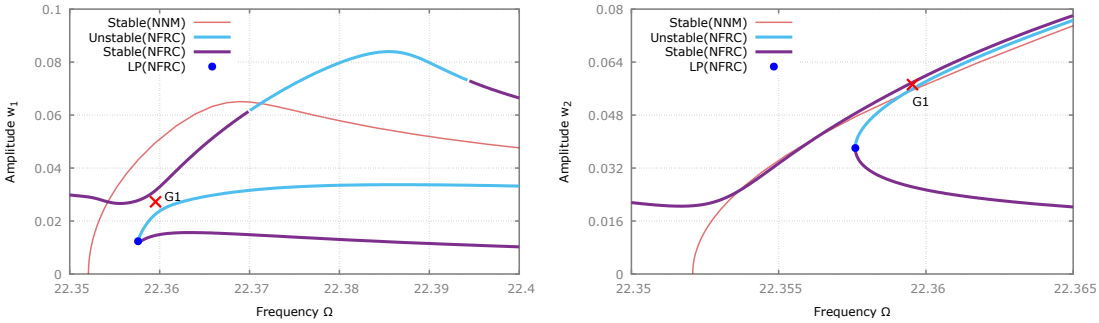

(c) Beam #1 (Zoom) (d) Beam #2 (Zoom)

Figure 13: Out-of-phase forcing ($d = 1.06$) - NFRCs after symmetry breaking ($\delta_m = 10^{-4}$ on beam #1). In accordance with Fig. 12d, for this level of forcing $d = 1.06$ the IS on the in-phase NNM branch has merged with the main NFRC.

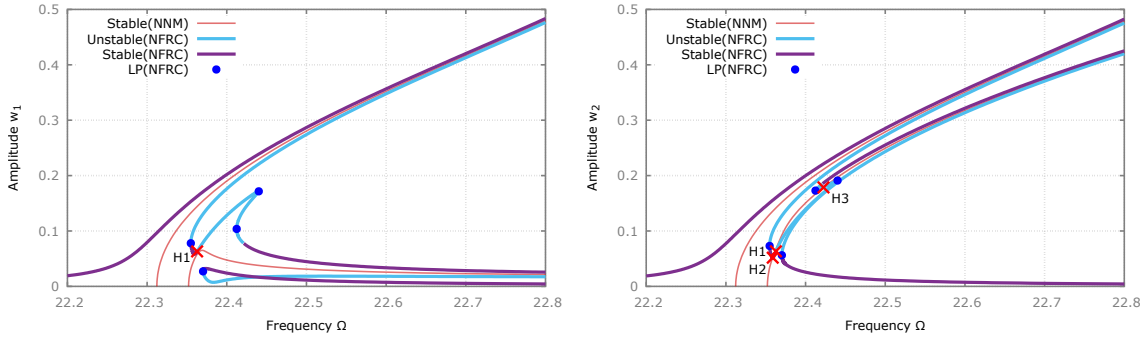

(a) Beam #1 (b) Beam #2

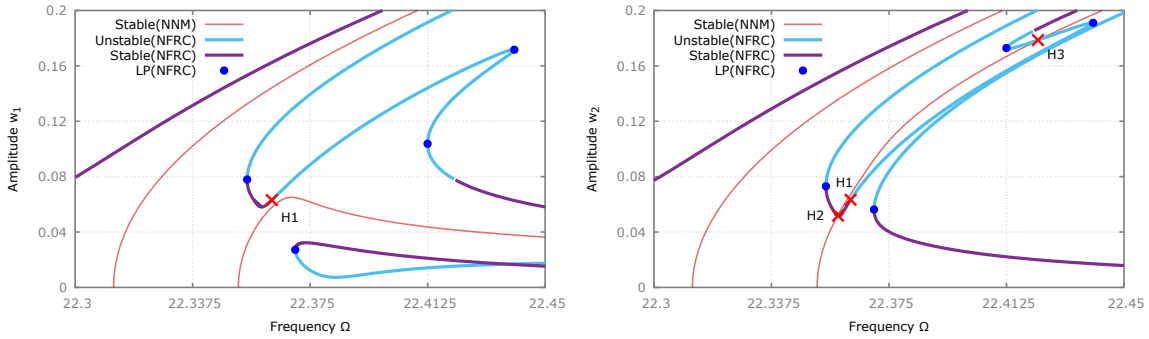

(c) Beam #1 (Zoom) (d) Beam #2 (Zoom)

Figure 14: Out-of-phase forcing ($d = 2.45$) - NFRCs after symmetry breaking ($\delta_m = 10^{-4}$ on beam #1)

the NFRCs supported by the in-phase NNM. For beam #1 the solutions supported by the in-phase NNM stay at low amplitude. On the other hand, for beam #2, the amplitude of the response increases with increased frequency.

In Fig. 14, the NFRCs are computed with $d = 2.45$ to analyze the merging behavior predicted by the energy balance method. In Fig. 14c, the intersection of the IS with the in-phase NNM (point $C4$ of Fig. 11a) has merged with the intersection of the main response curve with the in-phase NNM (point $C6$ of Fig. 11a) near point $H1$. On Fig. 14d, the response curve and the NNM intersect at two additional points ($H2, H3$). However, these points do not appear on the NFRC of beam #1 (see Fig. 14c). Therefore, points ($H2, H3$) do not represent solutions in phase quadrature. Only the merging point $H1$ is present on both NFRCs. For this reason, point $H1$ represents the merging of solutions in phase quadrature found with the energy balance method in Fig. 10.

Consequently, it can be concluded that the energy balance and the LP tracking reveal two different types of merging points. The LP tracking gives information on the merging of LPs located on ISs and on the main NFRC, while the energy balance gives information on the merging of solutions in phase quadrature.

4.3. Localization of motion with in-phase forcing

In order to detect and initialize the ISs supported by the INNM of Fig. 7, the in-phase electrostatic forcing defined in Table 1 is used to perform the energy balance presented in Fig. 15. Four points ($I1, I2, I3, I4$) are obtained for $d = 1$. Points $I1$ and $I2$ belong to the INNM, point $I3$ to the in-phase NNM, and the lowest point $I4$ to the out-of-phase NNM. The amplitude of point $I4$ is very small because the out-of-phase NNM is only slightly excited in this case of in-phase forcing. It can be observed that the birth of ISs takes place at a much lower forcing amplitude ($d \simeq 0.25$) than in the case of out-of-phase forcing ($d \simeq 0.6$, see Fig. 10). The ISs of Fig. 16 are initialized with the two points $I1$ and $I2$ obtained for $d = 1$ in Fig. 15. Due to the in-phase forcing, the ISs are supported by the entire INNM and not just by its stable part as in the case of out-of-phase forcing (Fig. 11). It is worth mentioning that point $I4$ of Fig. 16 is not the exact intersection of the main NFRC with the out-of-phase NNM because the main NFRC is composed of the modal contributions of both out-of-phase and in-phase NNMs.

For beam #1, the ISs have a high amplitude, whereas the main NFRC has a low amplitude. It is the opposite for beam #2: the main NFRC has a high amplitude, whereas the stable parts of the ISs have a low amplitude. Consequently, the phenomenon of localization of motion is more pronounced in the case of in-phase forcing than in the case of out-of-phase forcing.

5. Alternative methods for mass sensing

In this section, phenomena such as localization of motion and merging of ISs are exploited to propose alternative methods for mass sensing. Let's assume that there is some initial asymmetry in the beam array, either intentionally or due to manufacturing defects. By adding a mass larger than a specific threshold compensating the asymmetry, a symmetry breaking event will occur, leading to an inversion of localization. This inversion of localization can be used as a switch to enable mass detection. Two additional thresholds based on the merging of ISs can be combined with the inversion of localization in the case of out-of-phase forcing. A frequency sweep is used to reset the localization of motion in case of jumps to unwanted solutions such as ISs or solutions supported by the out-of-phase NNM. In the first part of this section, the case of out-of-phase forcing is considered. The corresponding sensing method is interesting because it involves two detection thresholds. These two thresholds are based on the inversion of localization and on the merging of ISs supported by the in-phase NNM with the main NFRC. The only drawback of this method is that the minimum frequency used during the frequency sweep is imposed. In the second part of this section, the case of in-phase forcing is considered. The corresponding sensing method involves only one threshold related to the inversion of localization but does not have the drawback of the method based on out-of-phase forcing. The generalization of this method to a n-beam MEMS array seems to be more promising for parallel mass detection.

5.1. Alternative mass sensing in the case of out-of-phase forcing

A parametric analysis with respect to the dimensionless added mass is first performed by means of LP tracking in order to highlight interesting features in the dynamics of the beam array that could be exploited for mass detection. Because the IS branches supported by the in-phase NNM and the INNM are always disconnected even in the perfectly

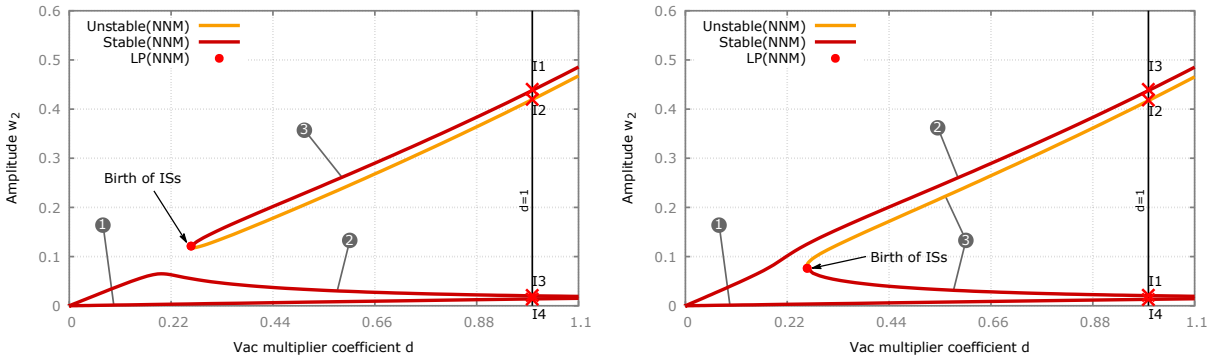

(a) Beam #1 (b) Beam #2

Figure 15: In-phase forcing - Energy balance after symmetry breaking ($\delta_m = 10^{-4}$ on beam #1). ❶: out-of-phase NNM, ❷: in-phase NNM, ❸: isolated NNM.

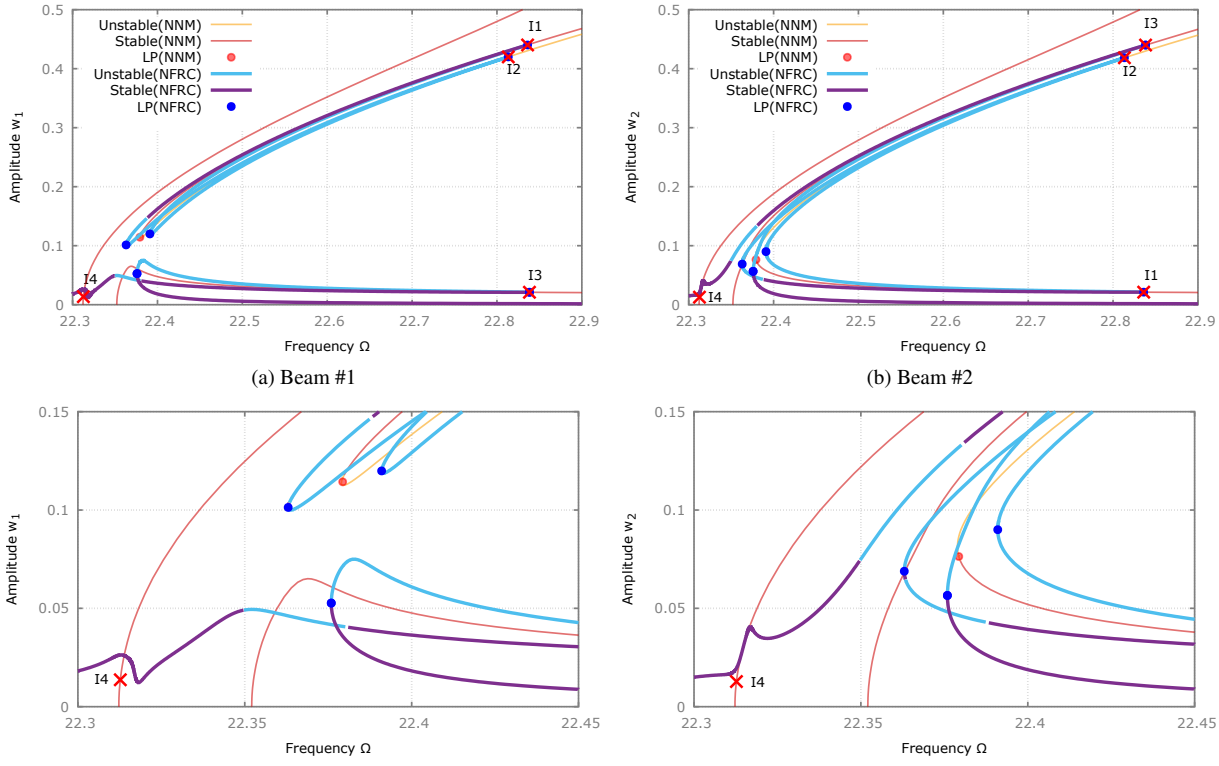

(a) Beam #1 (b) Beam #2

(c) Beam #1 (zoom) (d) Beam #2 (zoom)

Figure 16: In-phase forcing ($d = 1$) - NFRCs and ISs after symmetry breaking ($\delta_m = 10^{-4}$ on beam #1)

symmetric case ($\delta_m = 0$), two LP trackings with respect to δ_m are necessary to obtain all LP branches: the first one starting from $\delta_m > 0$ and the second one from $\delta_m < 0$.

The first LP tracking is initialized with LP F1 detected on the NFRC computed for $\delta_m = 10^{-4}$, as plotted in Fig. 17, and the branch of LPs is continued for increasing then decreasing values of δ_m. In Fig. 18, this LP tracking is plotted in the δ_m-Ω plane. The horizontal line $\delta_m = 10^{-4}$ is crossed by the LP branch at two additional points ($F2, F3$). These points can be used to initialize the IS supported by the pure in-phase NNM, see Figs. 17a and 17b. On the zoom of Fig. 18b, the birth of ISs supported by the INNM occurs for $\delta_m \simeq -5.65 \times 10^{-3}$. For δ_m lower than this value, the system is too much asymmetric for ISs to exist. The merging of ISs with the main NFRC occurs for $\delta_m \simeq 1.21 \times 10^{-4}$.

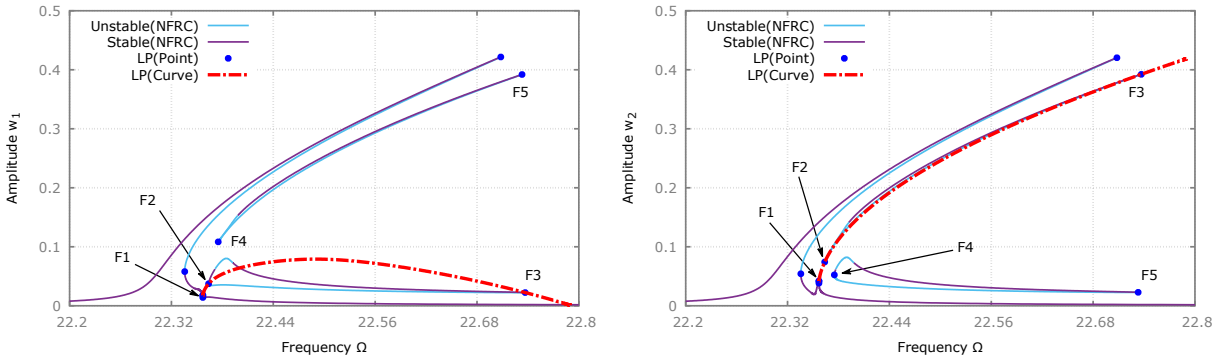

(a) Beam #1 (b) Beam #2

Figure 17: Out-of-phase forcing ($d = 1$) - LP tracking with respect to δ_m initialized with point F1 of Fig. 12

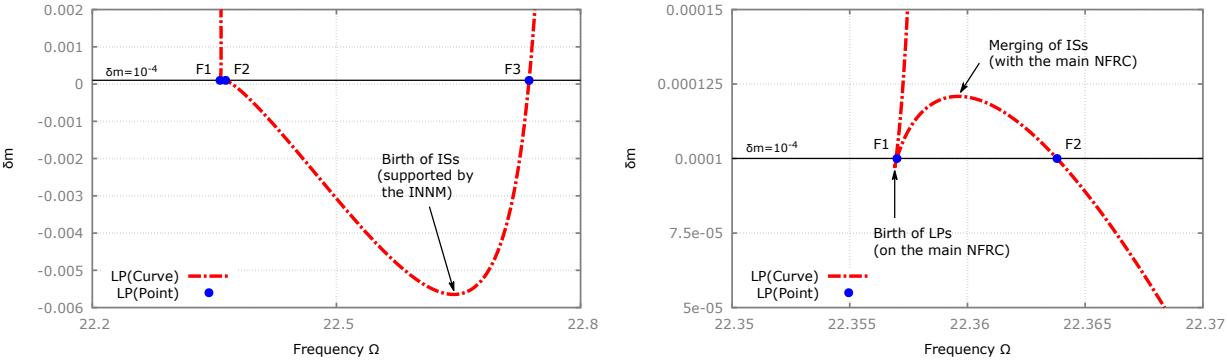

(a) LP tracking in the δ_m-Ω plane (b) Zoom

Figure 18: Out-of-phase forcing ($d = 1$) - LP tracking of Fig. 17 in the δ_m-Ω plane

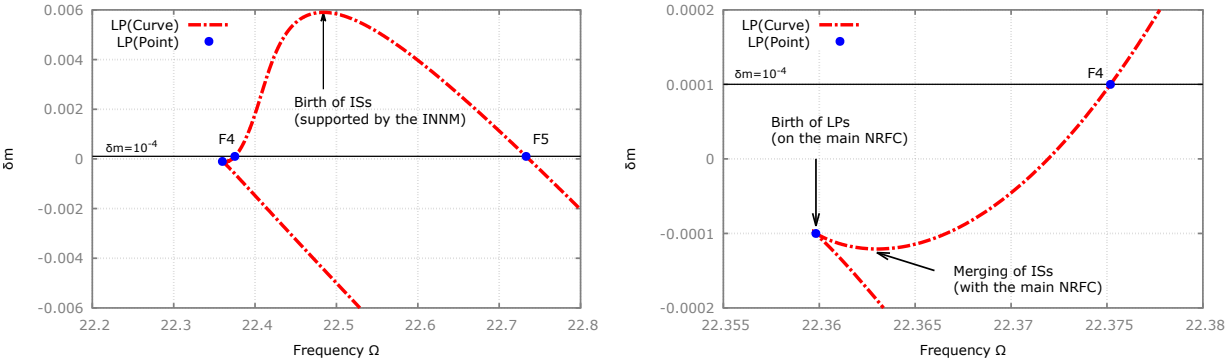

(a) LP tracking in the δ_m-Ω plane (b) Zoom

Figure 19: Out-of-phase forcing ($d = 1$) - LP tracking in the δ_m-Ω plane initialized with a LP on the main NRFC computed for $\delta_m = -10^{-4}$

For lower positive values of δ_m, the LPs are localized on the main NFRC and the IS supported by the pure in-phase NNM. For values of δ_m larger than this threshold, the level of asymmetry is such that the in-phase NNM is sufficiently excited for the ISs and the main NFRC to merge. Therefore, ISs can connect to the main NFRC by increasing the asymmetry of the system.

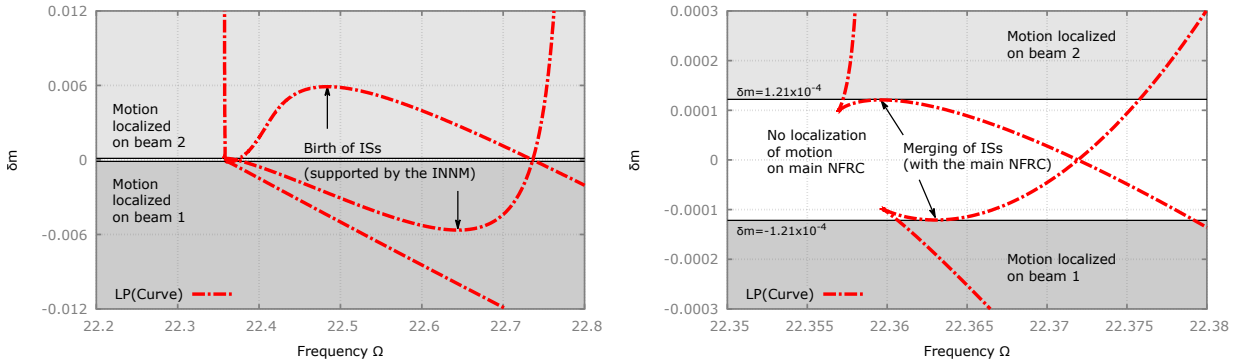

(a) LP tracking in the δ_m-Ω plane

(b) Zoom

Figure 20: Out-of-phase forcing ($d = 1$) - LP tracking of Figs. 17 and 19 in the δ_m-Ω plane

The second LP tracking is initialized with a LP detected on the NFRC computed for $\delta_m = -10^{-4}$. It is plotted in the δ_m-Ω plane in Fig. 19. The horizontal line $\delta_m = 10^{-4}$ is crossed twice by the LP branch at points $(F4, F5)$ which can be used to initialized the IS supported by the INNM in Fig. 17. In the zoom of Fig. 19b, the birth of ISs occurs for $\delta_m \simeq 5.65 \times 10^{-4}$. For higher values of δ_m, the system is too much asymmetric for ISs to exist. The merging of ISs with the main NFRC occurs for $\delta_m \simeq -1.21 \times 10^{-4}$. For lower values of δ_m, the level of asymmetry is such that the in-phase NNM is sufficiently excited for the ISs and the main NFRC to merge. For higher negative values of δ_m, LPs are located on the main NFRC and on the ISs supported by the in-phase NNM. For $\delta_m > 0$, LPs are located on the ISs supported by the INNM. For a better overview, the two LP trackings are plotted together in Fig. 20. Three different regions can be distinguished, one region with no localization of motion on the main NFRC and two regions with localized motion. For $\delta_m > 1.21 \times 10^{-4}$, the motion is localized on beam #2, whereas it is localized on beam #1 for $\delta_m < -1.21 \times 10^{-4}$. For $-1.21 \times 10^{-4} < \delta_m < 1.21 \times 10^{-4}$, there is no localization of motion on the main NFRC and two ISs can be observed (see Fig. 11 for instance).

The principle of mass detection proposed here is closely related to the three regions defined Fig. 20b and is based on a switch from one region to another in order to generate an inversion of localization. This is equivalent to a switch from the first imperfect bifurcation of Fig. 8b to the second one. To this end, an initial configuration in the upper region of Fig. 20b is considered, e.g., for $\delta_m = 1.4 \times 10^{-4}$. The corresponding NFRCs are plotted in Fig. 21. It can be observed that the ISs have merged with the main NFRCs as expected. For solutions on the merged ISs, beam #1 has a small amplitude, whereas beam #2 has a large amplitude, thus confirming the localization of motion on beam #2. By sweeping the frequency up and down alternately from $\Omega = 22.35$ to $\Omega = 22.8$, the localization of motion can be clearly observed since beam #1 has a small amplitude while beam #2 exhibits a hysteretic cycle with large jumps in amplitude. The minimum frequency of the frequency sweep must be chosen carefully: it must be between the frequencies of the two left-most LPs in Figs. 21a and 21b. Theoretically, the frequency sweep may not be mandatory, i.e., a fixed operating frequency should work as well. However, jumps to the upper out-of-phase NFRC may occur in experimental conditions. In this case, the frequency sweep ensures that the process is reset and makes detection more robust. It is worth mentioning that the small unstable area on the merged ISs is due to the presence of non-displayed Neimark-Sacker bifurcations and does not interfere with the frequency sweep-up.

When the additional mass δ_m is changed (removing mass on beam #1 is equivalent to adding mass on beam #2), three scenarios are possible:

- If δ_m remains in the upper region of Fig. 20b, i.e., $\delta_m > 1.21 \times 10^{-4}$, the overall behavior is unchanged and the motion remains localized on beam #2.
- If $-1.21 \times 10^{-4} < \delta_m < 1.21 \times 10^{-4}$ (central region of Fig. 20b), there is no localization of motion anymore since the solutions remain on the lower part of the main NFRC for beams #1 and #2 during the frequency sweep, as shown in Fig. 22. This change of behavior can be used as a first threshold indicating that $|\delta_m| < 1.21 \times 10^{-4}$.
- If $\delta_m < -1.21 \times 10^{-4}$ (lower region of Fig. 20b), there is an inversion of localization and the motion is now localized on beam #1, as shown in Fig. 23. This change of behavior can be used as a second threshold.

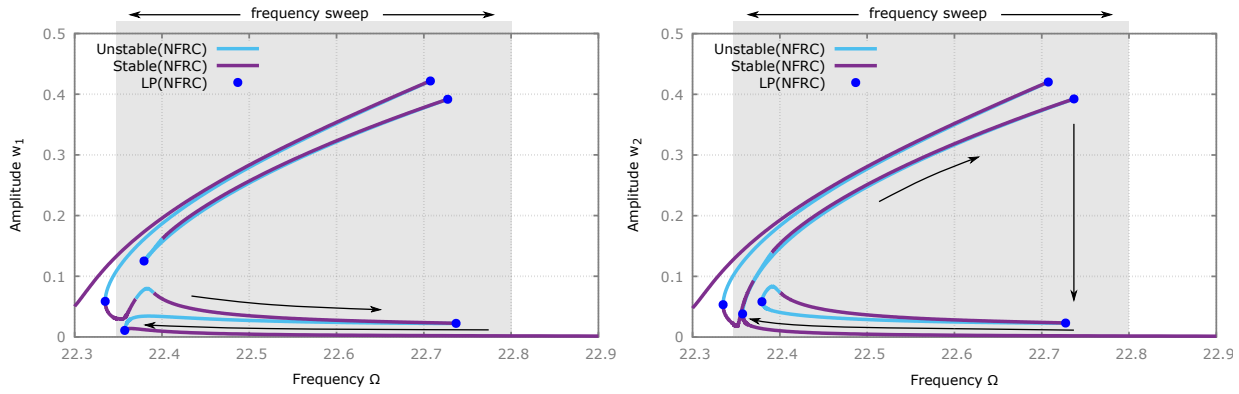

(a) Beam #1 (b) Beam #2

Figure 21: Out-of-phase forcing ($d = 1$) - NFRCs for in initial asymmetric configuration ($\delta_m = 1.4 \times 10^{-4}$ on beam #1). Motion is localized on beam #2

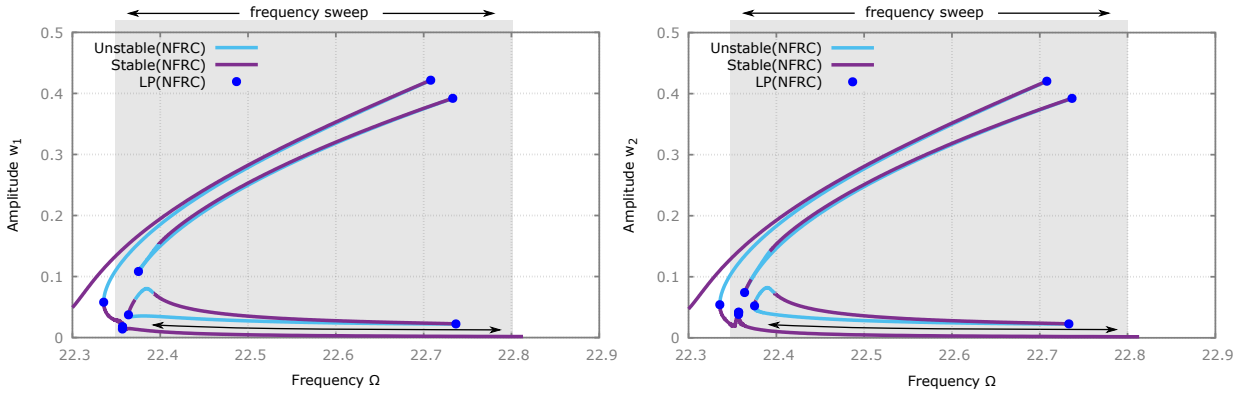

(a) Beam #1 (b) Beam #2

Figure 22: Out-of-phase forcing ($d = 1$) - NFRCs for modified additional mass ($\delta_m = 10^{-4}$ on beam #1). With this amount of added mass, no localization of motion is observed anymore for beam #2

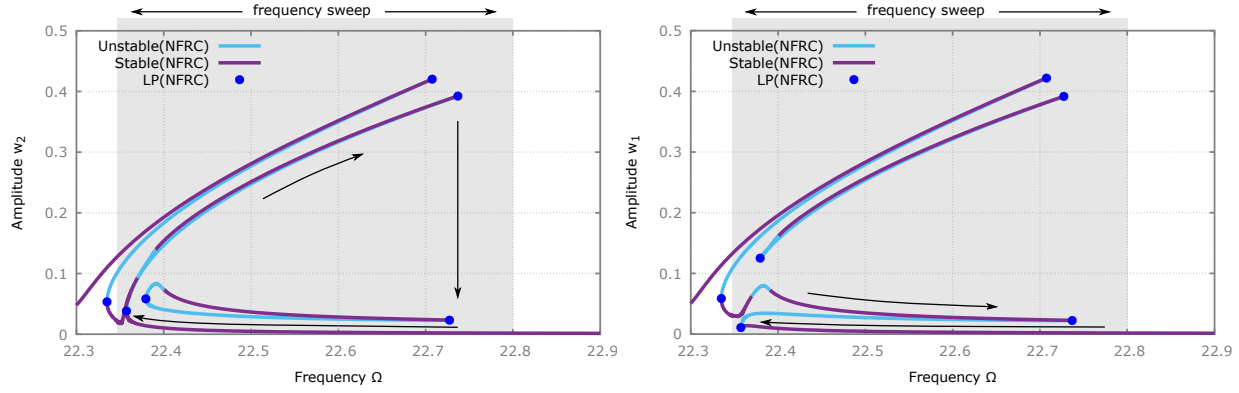

(a) Beam #1 (b) Beam #2

Figure 23: Out-of-phase forcing ($d = 1$) - NFRCs for modified additional mass ($\delta_m = -1.4 \times 10^{-4}$ on beam #1). This amount of added mass leads to an inversion of localization and the motion is now localized on beam #1

Thus, monitoring the changes of localization of motion gives indications on the variations of the additional mass. The threshold $|\delta_m| = 1.21 \times 10^{-4}$ generating the changes of behavior corresponds to the merging of ISs and is closely related to the level of asymmetry in the beam array. It can be adjusted by tuning the bias voltage V_{dc} [15], by changing the geometry of one of the two beams, or by adding a small amount of in-phase forcing. Offsetting this threshold is equivalent to changing the initial configuration, i.e., the initial value of δ_m used as a reference for the mass detection. The value $|\delta_m| \simeq 5.65 \times 10^{-4}$ corresponding to the birth of ISs can also be used as a supplementary threshold.

5.2. *Alternative mass sensing in the case of in-phase forcing*

The in-phase electrostatic forcing defined in Table 1 is now considered. In this case, all possible positions of the LPs when δ_m varies can be obtained with a single LP tracking. In Fig. 24, the main NFRC was computed for $\delta_m = 10^{-4}$. Then, the LP tracking was initialized with the LP L1. It is plotted in the δ_m-Ω plane in Fig. 25. The horizontal line $\delta_m = 10^{-4}$ is crossed by the LP branch at two additional points ($L2, L3$) which can be used to initialize the IS supported by the INNM of Figs. 24a and 24b. In the upper light gray region corresponding to $\delta_m > 0$, the motion is localized on beam #2, whereas it is localized on beam #1 in the lower dark gray region corresponding to $\delta_m < 0$.

As the case of out-of-phase forcing, the principle of mass detection is based on a switch from one region to another in order to generate an inversion of localization, but its implementation is simpler in the case of in-phase forcing since only two regions are involved. An asymmetric initial configuration in the upper region of Fig. 25 is considered. Such a configuration is obtained either by adding mass on beam #1, or by removing mass on beam #2, or by tuning the bias voltage V_{dc} [15]. With an additional mass $\delta_m = 10^{-4}$ on beam #1, the NFRCs and ISs of Fig.

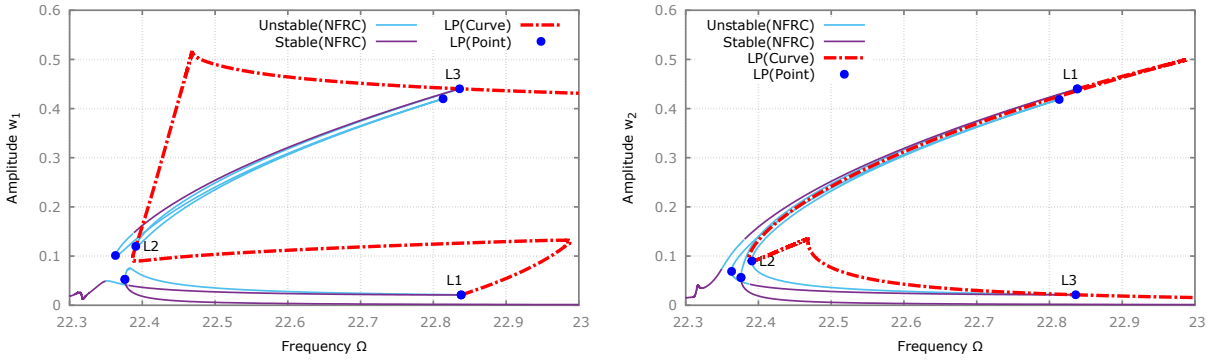

(a) Beam #1

(b) Beam #2

Figure 24: In-phase forcing ($d = 1$) - LP tracking with respect to δ_m initialized with point L1 of the main NRFC computed for $\delta_m = 10^{-4}$ on beam #1

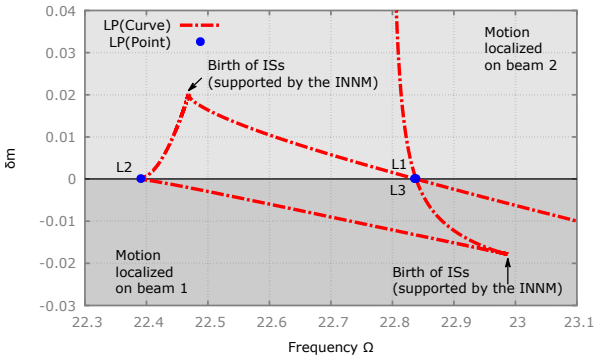

Figure 25: In-phase forcing ($d = 1$) - LP tracking of Fig. 24 in the δ_m-Ω plane

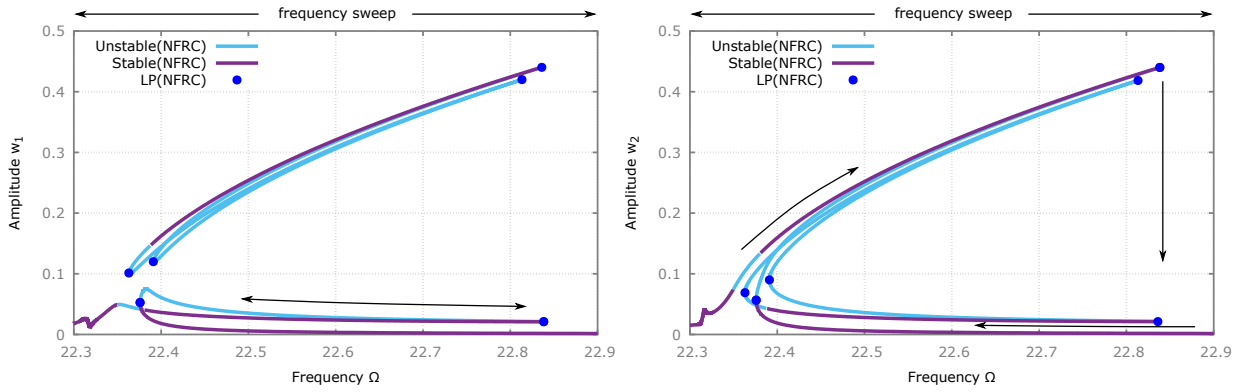

(a) Beam #1 (b) Beam #2

Figure 26: In-phase forcing ($d = 1$) - NFRCs for an initial asymmetric configuration ($\delta_m = 10^{-4}$ on beam #1). Motion is localized on beam #2

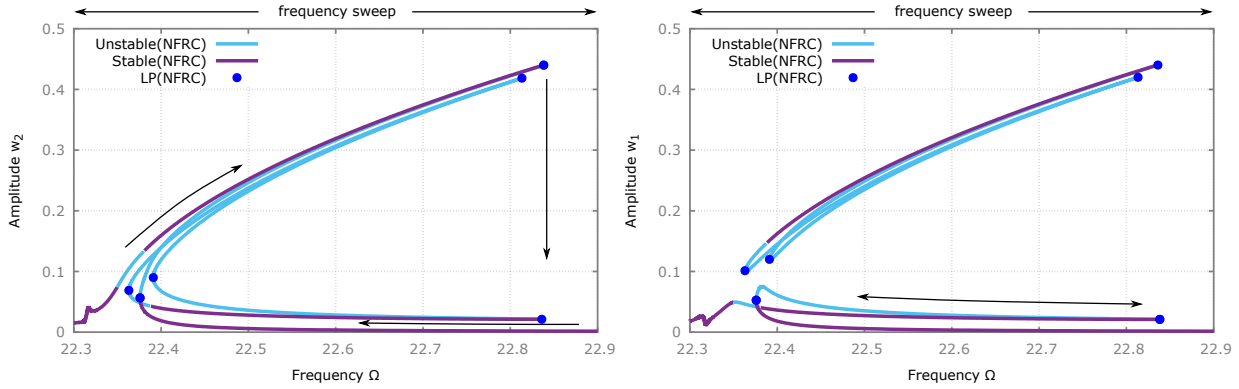

(a) Beam #1 (b) Beam #2

Figure 27: In-phase forcing ($d = 1$) - NFRCs for modified additional mass ($\delta_m = -10^{-4}$ on beam #1). This amount of added mass leads to an inversion of localization and the motion is now localized on beam #1

26 are obtained, where a localization of motion on beam #2 can be observed as expected. Since jumps to ISs may occur in experimental conditions, an alternating frequency sweep $22.3 \leq \Omega \leq 22.9$ is used to ensure that the process is reset after a jump. Contrary to the out-of-phase case, the boundaries of the frequency sweep are not imposed, they just have to be respectively lower and higher than the LPs of the ISs. During the frequency sweep, beam #1 keeps a small amplitude while beam #2 exhibits a hysteretic cycle with large jumps in amplitude.

If δ_m is modified so that $\delta_m < 0$, for example by removing mass on beam #1 or by adding mass on beam #2, an inversion of localization occurs and the motion is now localized on beam #1 instead of beam #2, as shown in Fig. 27. The amount of mass that can be detected by this method is directly related to the level of initial asymmetry. As already explained, this initial asymmetry can be adjusted by tuning the bias voltage V_{dc} [15], by adding a small amount of mass on one of the two beams, or by changing their geometry.

This alternative method could be generalized to larger arrays of MEMS resonators for achieving parallel mass detection. In [46, 47], the authors have found a pure NNM supporting successive mixed NNMs and BPs associated with symmetry breaking phenomena. By exciting these pure NNMs, each symmetry breaking could be used as an adjustable threshold for mass detection. Moreover, all the NNMs associated with these symmetry breakings are orthogonal to each others. Consequently, the thresholds associated to each of those symmetries are locally independent, making their tuning easier.

6. Conclusions

In this paper, a mass detection method based on symmetry breaking and localization of motion in an array of two MEMS resonators has been proposed.

The global dynamic of the MEMS array has been investigated using nonlinear normal modes (NNMs), nonlinear forced response curves and bifurcation tracking. In a perfectly symmetric configuration, it has been shown that NNMs are either pure or mixed NNMs. Mixed NNMs are bifurcated asymmetric solutions emanating from bifurcation points located on pure NNMs. The possible coexistence of isolated solutions is explained by means of energy balance and limit point tracking. The results show that the energy balance method and limit point tracking can be used equivalently to detect the birth of isolated solutions, but only the LP tracking can predict accurately their merging.

An additional mass generates a symmetry breaking that transforms mixed and symmetric pure NNMs into isolated NNMs and asymmetric pure NNMs. It also generates a localization of motion characterized by a larger vibratory amplitude on one of the two beams. When the additional mass becomes higher than an adjustable threshold, an inversion of localization occurs which can be used for mass detection. The amount of mass that can be detected by this method is directly related to the initial asymmetry level. It can be adjusted by tuning the bias voltage, by adding a small amount of mass on one of the two beams, or by changing their geometry.

Declaration of competing interest

The authors declare that they have no known competing financial interests or personal relationships that could have appeared to influence the work reported in this paper.

References

[1] M. Calleja, P. M. Kosaka, Á. San Paulo, J. Tamayo, Challenges for nanomechanical sensors in biological detection, Nanoscale 4 (2012) 4925–4938, doi:10.1039/c2nr31102j.

[2] Y. T. Yang, C. Callegari, X. L. Feng, K. L. Ekinci, M. L. Roukes, Zeptogram-scale nanomechanical mass sensing, Nano Lett. 6 (2006) 583–586, doi:10.1021/nl052134m.

[3] M. I. Younis, F. Al Saleem, Exploration of new concepts for mass detection in electrostatically-actuated structures based on nonlinear phenomena, J. Comput. Nonlinear Dyn. 4 (2009) 021010, doi:10.1115/1.3079785.

[4] J. F. Rhoads, S. W. Shaw, K. L. Turner, Nonlinear dynamics and its applications in micro- and nanoresonators, J. Dyn. Syst. Meas. Contr. 132 (2010) 034001, doi:10.1115/1.4001333.

[5] S. Baglio, A. R. Bulsara, B. Ando, S. L. Malfa, V. Marletta, C. Trigona, P. Longhini, A. Kho, V. In, J. D. Neff, G. W. Anderson, C. C. Obra, B. K. Meadows, A. Palacios, Exploiting nonlinear dynamics in novel measurement strategies and devices: From theory to experiments and applications, IEEE Trans. Instrum. Meas. 60 (2011) 667–695, doi:10.1109/tim.2010.2089576.

[6] S. Tiwari, R. N. Candler, Using flexural MEMS to study and exploit nonlinearities: a review, J. Micromech. Microeng. 29 (2019) 083002, doi:10.1088/1361-6439/ab23e2.

[7] L. Li, W. Zhang, J. Wang, K. Hu, B. Peng, M. Shao, Bifurcation behavior for mass detection in nonlinear electrostatically coupled resonators, Int. J. Non Linear Mech. 119 (2020) 103366, doi:10.1016/j.ijnonlinmec.2019.103366.

[8] N. Alcheikh, S. Ben. Mbarek, H. M. Ouakad, M. I. Younis, A highly sensitive and wide-range resonant magnetic micro-sensor based on a buckled micro-beam, Sensors and Actuators A: Physical 328 (2021) 112768, doi:10.1016/j.sna.2021.112768.

[9] V. N. Nguyen, S. Baguet, C.-H. Lamarque, R. Dufour, Bifurcation-based micro-/nanoelectromechanical mass detection, Nonlinear Dyn. 79 (2015) 647–662, doi:10.1007/s11071-014-1692-7.

[10] E. Buks, M. L. Roukes, Electrically tunable collective response in a coupled micromechanical array, J. Microelectromech. Syst. 11 (2002) 802–807, doi:10.1109/JMEMS.2002.805056.

[11] R. Lifshitz, M. C. Cross, Response of parametrically driven nonlinear coupled oscillators with application to micromechanical and nanomechanical resonator arrays, Phys. Rev. B 67 (2003) 134302, doi:10.1103/PhysRevB.67.134302.

[12] M. C. Cross, A. Zumdieck, R. Lifshitz, J. L. Rogers, Synchronization by nonlinear frequency pulling, Phys. Rev. Lett. 93 (2004) 224101, doi:10.1103/PhysRevLett.93.224101.

[13] D. Platz, U. Schmid, Vibrational modes in MEMS resonators, Journal of Micromechanics and Microengineering 29 (2019) 123001, doi:10.1088/1361-6439/ab4bad.

[14] R. Lifshitz, E. Kenig, M. C. Cross, Collective dynamics in arrays of coupled nonlinear resonators, in: Fluctuating Nonlinear Oscillators, Oxford University Press, 2012, pp. 278–311, doi:10.1093/acprof:oso/9780199691388.003.0011.

[15] M. Porfiri, Vibrations of parallel arrays of electrostatically actuated microplates, Journal of Sound and Vibration 315 (2008) 1071–1085, doi:10.1016/j.jsv.2008.02.007.

[16] S. Gutschmidt, O. Gottlieb, Internal resonances and bifurcations of an array below the first pull-in instability, International Journal of Bifurcation and Chaos 20 (2010) 605–618, doi:10.1142/s0218127410025910.

[17] S. Gutschmidt, O. Gottlieb, Nonlinear dynamic behavior of a microbeam array subject to parametric actuation at low, medium and large DC-voltages, Nonlinear Dyn. 67 (2012) 1–36, doi:10.1007/s11071-010-9888-y.

[18] D. Bitar, N. Kacem, N. Bouhaddi, M. Collet, Collective dynamics of periodic nonlinear oscillators under simultaneous parametric and external excitations, Nonlinear Dyn. 82 (2015) 749–766, doi:10.1007/s11071-015-2194-y.
[19] D. Bitar, N. Kacem, N. Bouhaddi, Multistability and bifurcation topology in electrostatically coupled nanobeams under parametric resonance, in: ASME 2017 International Design Engineering Technical Conferences and Computers and Information in Engineering Conference, 2017, pp. DETC2017–67588, doi:10.1115/detc2017-67588.
[20] P. N. Kambali, F. Torres, N. Barniol, O. Gottlieb, Nonlinear multi-element interactions in an elastically coupled microcantilever array subject to electrodynamic excitation, Nonlinear Dyn. 98 (2019) 3067–3094, doi:10.1007/s11071-019-05074-7.
[21] T. L. Hill, S. A. Neild, A. Cammarano, An analytical approach for detecting isolated periodic solution branches in weakly nonlinear structures, J. Sound Vib. 379 (2016) 150–165, doi:10.1016/j.jsv.2016.05.030.
[22] R. J. Kuether, L. Renson, T. Detroux, C. Grappasonni, G. Kerschen, M. S. Allen, Nonlinear normal modes, modal interactions and isolated resonance curves, J. Sound Vib. 351 (2015) 299–310, doi:10.1016/j.jsv.2015.04.035.
[23] L. L. Li, P. M. Polunin, S. Dou, O. Shoshani, B. Scott Strachan, J. S. Jensen, S. W. Shaw, K. L. Turner, Tailoring the nonlinear response of MEMS resonators using shape optimization, Appl. Phys. Lett. 110 (2017) 081902, doi:10.1063/1.4976749.
[24] M. S. Hajhashemi, A. Amini, B. Bahreyni, A micromechanical bandpass filter with adjustable bandwidth and bidirectional control of centre frequency, Sensors and Actuators A: Physical 187 (2012) 10–15, doi:10.1016/j.sna.2012.08.008.
[25] V. Walter, G. Bourbon, P. Le Moal, N. Kacem, J. Lardiès, Electrostatic actuation to counterbalance the manufacturing defects in a MEMS mass detection sensor using mode localization, Procedia Engineering 168 (2016) 1488–1491, doi:10.1016/j.proeng.2016.11.431.
[26] P. N. Kambali, G. Swain, A. K. Pandey, E. Buks, O. Gottlieb, Coupling and tuning of modal frequencies in direct current biased microelectromechanical systems arrays, Appl. Phys. Lett. 107 (2015) 063104, doi:10.1063/1.4928536.
[27] M. Akgul, Z. Ren, C. T.-C. Nguyen, Voltage-controlled tuning to optimize MEMS resonator array-composite output power, in: Frequency Control and the European Frequency and Time Forum (FCS), 2011 Joint Conference of the IEEE International, 2011, pp. 1–6, doi:10.1109/fcs.2011.5977901.
[28] M. Spletzer, A. Raman, H. Sumali, J. P. Sullivan, Highly sensitive mass detection and identification using vibration localization in coupled microcantilever arrays, Appl. Phys. Lett. 92 (2008) 114102, doi:10.1063/1.2899634.
[29] H. Pakdast, M. Lazzarino, Triple coupled cantilever systems for mass detection and localization, Sens. Actuators, A 175 (2012) 127–131, doi:10.1016/j.sna.2011.12.032.
[30] M. Manav, G. Reynen, M. Sharma, E. Cretu, A. S. Phani, Ultrasensitive resonant MEMS transducers with tuneable coupling, J. Micromech. Microeng. 24 (2014) 055005, doi:10.1088/0960-1317/24/5/055005.
[31] J.-R. Liu, Y.-C. Lo, W.-C. Li, A novel micromechanical mode-localized resonator utilizing anti-resonating structures, in: 2019 IEEE 32nd International Conference on Micro Electro Mechanical Systems (MEMS), 2019, doi:10.1109/memsys.2019.8870834.
[32] T. Rabenimanana, V. Walter, N. Kacem, P. Le Moal, G. Bourbon, J. Lardiès, Mass sensor using mode localization in two weakly coupled MEMS cantilevers with different lengths: Design and experimental model validation, Sens. Actuators, A 295 (2019) 643–652, doi:10.1016/j.sna.2019.06.004.
[33] A. Z. Hajjaj, N. Jaber, S. Ilyas, F. K. Alfosail, M. I. Younis, Linear and nonlinear dynamics of micro and nano-resonators: Review of recent advances, Int. J. Non Linear Mech. 119 (2020) 103328, doi:10.1016/j.ijnonlinmec.2019.103328.
[34] S. Ilyas, M. I. Younis, Theoretical and experimental investigation of mode localization in electrostatically and mechanically coupled microbeam resonators, Int. J. Non Linear Mech. 125 (2020) 103516, doi:10.1016/j.ijnonlinmec.2020.103516.
[35] D. F. Wang, K. Chatani, T. Ikehara, R. Maeda, Mode localization analysis and characterization in a 5-beam array of coupled nearly identical micromechanical resonators for ultra-sensitive mass detection and analyte identification, Microsyst. Technol. 18 (2012) 1923–1929, doi:10.1007/s00542-012-1520-2.
[36] P. Thiruvenkatanathan, J. Yan, J. Woodhouse, A. A. Seshia, Enhancing parametric sensitivity in electrically coupled MEMS resonators, J. Microelectromech. Syst. 18 (2009) 1077–1086, doi:10.1109/jmems.2009.2025999.
[37] H. M. Ouakad, S. Ilyas, M. I. Younis, Investigating mode localization at lower- and higher-order modes in mechanically coupled MEMS resonators, J. Comput. Nonlinear Dyn. 15 (2020), doi:10.1115/1.4045634.
[38] C. Zhao, M. H. Montaseri, G. S. Wood, S. H. Pu, A. A. Seshia, M. Kraft, A review on coupled MEMS resonators for sensing applications utilizing mode localization, Sens. Actuators, A 249 (2016) 93–111, doi:10.1016/j.sna.2016.07.015.
[39] M. Lyu, J. Zhao, N. Kacem, P. Liu, B. Tang, Z. Xiong, H. Wang, Y. Huang, Exploiting nonlinearity to enhance the sensitivity of mode-localized mass sensor based on electrostatically coupled MEMS resonators, Int. J. Non Linear Mech. 121 (2020) 103455, doi:10.1016/j.ijnonlinmec.2020.103455.
[40] M. Alkaddour, M. Ghommem, F. Najar, Nonlinear analysis and effectiveness of weakly coupled microbeams for mass sensing applications, Nonlinear Dyn. 104 (2021) 383–397, doi:10.1007/s11071-021-06298-2.
[41] S. Baguet, V.-N. Nguyen, C. Grenat, C.-H. Lamarque, R. Dufour, Nonlinear dynamics of micromechanical resonator arrays for mass sensing, Nonlinear Dyn. 95 (2019) 1203–1220, doi:10.1007/s11071-018-4624-0.
[42] M. I. Younis, MEMS Linear and Nonlinear Statics and Dynamics, Springer US, 2011, doi:10.1007/978-1-4419-6020-7.
[43] L. Xie, S. Baguet, B. Prabel, R. Dufour, Bifurcation tracking by harmonic balance method for performance tuning of nonlinear dynamical systems, Mech. Syst. Sig. Process. 88 (2017) 445–461, doi:10.1016/j.ymssp.2016.09.037.
[44] C. Grenat, S. Baguet, R. Dufour, C.-H. Lamarque, Bifurcation analysis of nonlinear normal modes with the harmonic balance method, in: ENOC 2017, 9th European Nonlinear Dynamics Conference, Budapest, Hungary, 2017.
[45] M. Golubitsky, D. G. Schaeffer, Singularities and groups in bifurcation theory, volume 1, Springer Science & Business Media, 2012, doi:10.1007/978-1-4612-5034-0.
[46] A. Grolet, F. Thouverez, Free and forced vibration analysis of a nonlinear system with cyclic symmetry: Application to a simplified model, J. Sound Vib. 331 (2012) 2911 – 2928, doi:https://doi.org/10.1016/j.jsv.2012.02.008.
[47] A. Papangelo, F. Fontanela, A. Grolet, M. Ciavarella, N. Hoffmann, Multistability and localization in forced cyclic symmetric structures modelled by weakly-coupled duffing oscillators, J. Sound Vib. 440 (2019) 202 – 211, doi:https://doi.org/10.1016/j.jsv.2018.10.028.